

Fast 3D wave-equation migration-velocity analysis using the prestack exploding-reflector model

Claudio Guerra* and Biondo Biondi†

**Formerly Stanford Exploration Project, Geophysics Department, Stanford University,
Stanford, CA 94305. Presently Petrobras, Rio de Janeiro, Brazil.*

E-mail: claudio.guerra@petrobras.com.br

*†Stanford Exploration Project, Geophysics Department, Stanford University, Stanford, CA
94305. E-mail: biondo@sep.stanford.edu*

(November 9, 2010)

Running head: **WEMVA with the prestack exploding-reflector**

ABSTRACT

An accurate depth-velocity model is the key for obtaining good quality and reliable depth images in areas of complex geology. In such areas, velocity-model definition should use methods that describe the complexity of wavefield propagation, such as focusing and defocusing, multiple arrivals, and frequency-dependent velocity sensitivity. Wave-equation tomography in the image space has the ability to handle these issues because it uses wavefields as carriers of information. However, its high cost and low flexibility for parametrizing the model space has prevented its routine industrial use. This thesis aims at overcoming those limitations by using new wavefields as carriers of information: the image-space generalized wavefields. These wavefields are synthesized by using a pre-stack generalization of the exploding-reflector model. Cost of wave-equation tomography in the image space is

decreased because only a small number of image-space generalized wavefields are necessary to accurately describe the kinematics of velocity errors and because these wavefields can be easily used in a target-oriented way. Flexibility is naturally incorporated into wave-equation tomography in the image space by using these wavefields because their modeling have as the initial conditions some key selected reflectors, allowing a layer-based parametrization of the model space. To use the image-space generalized wavefields in wave-equation tomography in the image space, the method is extended from the shot-profile domain to the image-space generalized-sources domain. In this new domain, the velocity updates are very fast. Migration with the optimized velocity model provides good quality and reliable depth images, as can be seen in a 3D-field data example.

INTRODUCTION

PRESTACK EXPLODING-REFLECTOR MODEL

A prestack image computed with an inaccurate velocity model by wavefield-extrapolation methods presents energy departing from the zero subsurface offset. In conventional Born modeling, the entire prestack image is spatially convolved with the source wavefield, generating the receiver wavefield, whose back-propagation and collection at the surface originate data. In order to guarantee illumination similar to the original, several shot records need to be modeled. Notice that both source and receiver wavefields must be propagated with the same inaccurate velocity model used in the original migration to preserve the correct kinematics. Now, let us consider the modeling of data necessary to correctly image a single subsurface-offset common-image gather (SODCIG) of a reflector. Since we do not know beforehand which shots contribute to forming the image at a point in the subsurface, again we would have to perform several modeling experiments to synthesize these shot records. However, ideally, we would like to synthesize a small amount of data with the condition that migration produces the same kinematics of the initial prestack reflector. This is the fundamental idea of the prestack exploding-reflector model (PERM) (Biondi, 2006), whose primary objective is to accelerate migration-velocity analysis.

Areal data is generated by PERM, propagating energy of a prestack image. PERM operates in a way similar to the exploding-reflector model (ERM). However, since migration of PERM data can produce a prestack image, PERM can be considered a generalization of ERM. The modeling of PERM wavefields can be carried out by any wavefield-continuation

scheme. Here, we use the following one-way wave equations:

$$\begin{cases} \left(\frac{\partial}{\partial z} - i\sqrt{\omega^2 s_0^2(\mathbf{x}) - |\mathbf{k}|^2} \right) D(\mathbf{x}, \omega; \mathbf{x}_m) = I_D(\mathbf{x}_m, \mathbf{h}) \\ D(x, y, z = z_{\max}, \omega; \mathbf{x}_m) = 0 \end{cases}, \quad (1)$$

and

$$\begin{cases} \left(\frac{\partial}{\partial z} + i\sqrt{\omega^2 s_0^2(\mathbf{x}) - |\mathbf{k}|^2} \right) U(\mathbf{x}, \omega; \mathbf{x}_m) = I_U(\mathbf{x}_m, \mathbf{h}) \\ U(x, y, z = z_{\max}, \omega; \mathbf{x}_m) = 0 \end{cases}, \quad (2)$$

where ω is the radial frequency, s_0 is the same background velocity used to produce the initial prestack image, D and U represent the downward and the upward PERM wavefields, respectively, I_D and I_U are subsets of the prestack image centered at \mathbf{x}_m for a single reflector, suitable for the initial conditions for modeling downward and upward PERM wavefields, respectively. The information along the subsurface-offset \mathbf{h} dimension of the initial conditions is projected onto the \mathbf{x} dimension for the modeling. The subsurface offset is parameterized as $\mathbf{h} = (h_x, h_y)$, where h_x and h_y are the inline- and the crossline-subsurface offsets, respectively. Notice that if the prestack image has energy focused at zero subsurface offset, the initial conditions can be parameterized only by its spatial coordinates, and PERM is equivalent to ERM.

The initial conditions are obtained by rotating the original unfocused SODCIGs according to the apparent geological dip of the reflector. This operation corrects for the image-point dispersal due to velocity inaccuracy, causing events with different reflection angles from the same reflection point to be imaged at different locations. This is a consequence of not shifting the wavefields along the apparent geological-dip direction (Biondi and Symes, 2004) when applying the multi-offset image condition (Rickett and Sava, 2002). The 2D geometry that explains the rotation is depicted in Figure 1 for the cases of migration velocity which is slower (Figure 1a) and faster (Figure 1b) than the correct one.

The angles $\gamma + \alpha$ and $\gamma - \alpha$ are the source and receiver ray angles, respectively. They are the propagation directions of the wavefields locally at the image point. In 2D, α and γ are related to slopes in the pre-stack image according to

$$\tan \alpha = -\frac{dz_m}{dx_m} \quad (3)$$

$$\tan \gamma = -\frac{dz}{dh_x}, \quad (4)$$

where the subscript m in equation 3 refers to the local nature of the relationship. The solutions of the differential equations 3 and 4 define slant-stack paths, which allow us to transform the 2D pre-stack image $I(x, z, h_x)$ into $I(x, z, \alpha, \gamma)$. To align the initial conditions with the geological dip, the dip along the subsurface-offset axis is changed, yielding the new subsurface offset \widetilde{h}_{x_s} and \widetilde{h}_{x_r} for the initial conditions of the modeling of downward and upward PERM wavefields, respectively. This is accomplished by solving the following differential equations:

$$\tan(\gamma + \alpha) = -\frac{dz}{d\widetilde{h}_{x_s}}, \quad (5)$$

$$\tan(\gamma - \alpha) = \frac{dz}{d\widetilde{h}_{x_r}}. \quad (6)$$

The solutions of equations 5 and 6 define new slant-stack operations, which reduce the dimensionality of the decomposed pre-stack image by transforming $I(x, z, \alpha, \gamma)$ into $I_D(x, z, \widetilde{h}_{x_s})$ and $I_U(x, z, \widetilde{h}_{x_r})$. In 3D, the cross-line subsurface offsets also must be rotated. A complete description of the 3D rotation is given by Guerra (2010).

PERM as described by equations 1 and 2 generates sufficient data to image a single SODCIG. However, to fully image a reflector, we would have to model data that could potentially be even greater than the original data. Using the linearity of wavefield propagation, the modeling experiments can be combined in a way that PERM data size is decreased.

Hence, a group of SODCIGs equally spaced by certain x and y decorrelation distances is simultaneously injected into the modeling according to

$$\begin{cases} \left(\frac{\partial}{\partial z} - i\sqrt{\omega^2 s_0^2(\mathbf{x}) - |\mathbf{k}|^2} \right) \widehat{D}(\mathbf{x}, \omega) = \widehat{I}_D(\mathbf{x} - \mathbf{h}) \\ \widehat{D}(x, y, z = z_{\max}, \omega) = 0 \end{cases}, \quad (7)$$

and

$$\begin{cases} \left(\frac{\partial}{\partial z} + i\sqrt{\omega^2 s_0^2(\mathbf{x}) - |\mathbf{k}|^2} \right) \widehat{U}(\mathbf{x}, \omega) = \widehat{I}_U(\mathbf{x} + \mathbf{h}) \\ \widehat{U}(x, y, z = z_{\max}, \omega) = 0 \end{cases}, \quad (8)$$

where \widehat{I}_D and \widehat{I}_U are the combination of SODCIGs for a single reflector to be used as the initial conditions for the modeling of combined downward and upward wavefields, \widehat{D} and \widehat{U} , respectively. The selection of SODCIGs can be thought of as the multiplication of the pre-stack image by a 2D-comb function, which is shifted laterally to select new set of SODCIGs to initiate the modeling of another pair of combined wavefields. After shifting along one period of the sampling function in the x and y directions, all the points on the reflector are used in the modeling. Consequently, the number of modeling experiments equals the number of lateral shifts of the sampling function. If the periods of the 2D-comb function are chosen to be the decorrelation distances, no crosstalk between wavefields from different SODCIGs occurs during migration. The decorrelation distances correspond to twice the x and y subsurface-offset range. If more than one reflector is used, each reflector is separately injected into the modeling, so that wavefields from different reflectors do not cross-correlate during imaging, avoiding reflector crosstalk. These procedures to avoid crosstalk limit data size reduction with PERM. To overcome this limitation, two different strategies can be used, mitigating the effects of both kinds of crosstalk.

One strategy mitigates the reflector crosstalk, benefiting from the fact that the image of a reflector is formed at the zero time of wavefield propagation when the migration velocity

is accurate. When the migration velocity is inaccurate, the focusing of the image departs from the zero time, and this can be potentially used to update the velocity model (Sava and Fomel, 2006; Yang and Sava, 2009). Therefore, depending on the magnitude of the velocity errors and the distance between reflectors, selecting events with propagation time close to zero can avoid cross-correlating unrelated events. This is the principle of the time-windowed imaging condition, which for a single pair of PERM wavefields reads

$$I_w(\mathbf{x}, \mathbf{h}) = \sum_{-\frac{t_w}{2} \leq t \leq \frac{t_w}{2}} \mathcal{F}^{-1} \left[\widehat{D}^*(\mathbf{x} - \mathbf{h}) \right] \mathcal{F}^{-1} \left[\widehat{U}(\mathbf{x} + \mathbf{h}) \right], \quad (9)$$

where t_w is the length of the time window. When using one-way propagators, the wavefields are inverse Fourier transformed to time by \mathcal{F}^{-1} .

Another strategy is to phase-encode the modeling experiments. Phase-encoding is a well established technique for decreasing the cost of seismic imaging by linearly combining the shot records (Schultz and Claerbout, 1978; Whitmore, 1995; Romero et al., 2000; Sun et al., 2002; Liu et al., 2006; Duquet and Lailly, 2006). Phase-encoding is usually performed in the data space. However, wavefields can also be phase-encoded in the image space, using stochastic phase functions parametrized according to the model-space coordinates and selected reflector. Phase-encoding the modeling experiments mitigates not only reflector crosstalk but also crosstalk from different SODCIGs. This is achieved by phase-encoding the initial conditions \widetilde{I} , according to:

$$\widetilde{I}(\widehat{\mathbf{x}}, \mathbf{h}, \mathbf{q}, \omega) = \sum_m \sum_j \delta(\widehat{\mathbf{x}} - m\Delta\mathbf{x}) \beta(\widehat{\mathbf{x}}, j, \mathbf{q}, \omega) W_j(\widehat{\mathbf{x}}, \mathbf{h}) I(\widehat{\mathbf{x}}, \mathbf{h}), \quad (10)$$

where W_j selects the reflector j by identifying and windowing it in the pre-stack image I , and $\beta(\widehat{\mathbf{x}}, j, \mathbf{q}, \omega)$ is a pseudo-random phase-encoding function defined as

$$\beta(\widehat{\mathbf{x}}, j, \mathbf{q}, \omega) = e^{i\epsilon(\widehat{\mathbf{x}}, j, \mathbf{q}, \omega)}, \quad (11)$$

with $\epsilon(\widehat{\mathbf{x}}, j, \mathbf{q}, \omega)$ usually being a uniformly distributed pseudo-random sequence with zero mean. Sequences used in third- and fourth-generation cellphones can also be used to phase-encode the modeling (Guerra and Biondi, 2008). The pseudo-random phase-encoding function causes the frequency components of the initial conditions to be randomly injected into the modeling. Downward and upward image-space phase-encoded wavefields (ISPEW) initiated at the same SODCIG and from the same reflector are equally encoded, whereas downward and upward ISPEW initiated at different SODCIGs and from the different reflectors have different codes assigned to them. According to the law of large numbers, crosstalk attenuation is more effective for more random realizations.

PERM wavefields can be collected at any depth, which can be the top of a region of inaccurate velocity, having key reflectors within this region as the initial conditions. By doing so, velocity update will be restricted to the inaccurate velocity region. The use of key reflectors characterizes a target-oriented strategy to perform MVA by wavefield extrapolation. These two features along with the decrease of data size yielded by PERM drastically decreases the cost of MVA by wavefield extrapolation.

To illustrate the computation of PERM data and ISPEW, a prestack image computed with the inaccurate velocity model of Figure 2b is used as the initial conditions after rotation according the apparent geological dip. Data comprise 375 split-spread shots, with 6000 m maximum offset, computed by one-way Born modeling using the smooth Marmousi velocity model of Figure 2a along with the reflectivity derived from the true Marmousi model. The inaccurate velocity model is exactly the same as the correct velocity model up to the black horizon. From this horizon down, velocity is strongly smoothed and multiplied by 0.9. The curvature of the reflectors in the SODCIG and the pull-up of reflectors in the center of Figure 3a reflect the velocity inaccuracy. We use the four reflectors shown in Figure 3b to

model 35 pairs of PERM data (Figure 4) and 11 pairs of ISPEW (Figure 5). Migration of the 35 pairs of PERM data using the conventional imaging condition is shown in Figure 6a and using the time-windowed-imaging condition is shown in Figure 6b. Notice that crosstalk is almost completely avoided. Migration of the 11 pairs of ISPEW is shown in Figure 7. Reflectors are satisfactorily imaged and crosstalk is dispersed throughout the image.

Residual-moveout panels from images computed with the original shot records (Figure 8a), with 35 pairs of PERM data (Figure 8b), and with 11 ISPEW (Figure 8c) are used to analyze the quality of the moveout information. Notice that in the ADCIGs corresponding to images computed with PERM wavefields and ISPEWs, less events are present since we selected four reflectors to model these wavefields. The corresponding reflectors in the original shot-profile image are highlighted by the green boxes in Figure 8a. The residual moveout information in the four panels is very similar. However, some crosstalk not entirely rejected by the time-windowed imaging condition causes the residual-moveout information lose resolution in Figure 8b when compared to Figures 8c.

The cost for obtaining the images in Figure 8 widely varies. For instance, migrating 11 ISPEW is approximately 30 times faster than migrating all the 375 original shots. Using the same wavefields, computing the gradient of the objective function of MVA by wavefield-extrapolation can be 60 times faster. This difference in performance is even more dramatic when we consider that several iterations of migrations and gradient computations are performed during migration-velocity optimization by wavefield-extrapolation.

MVA BY WAVEFIELD-EXTRAPOLATION

Optimization of the migration velocity is a non-linear inverse problem. When using wavefield-extrapolation methods, it searches for an optimal background velocity which minimizes an objective function defined in the image space. The residual that characterizes the objective function is represented by the perturbed image $\Delta\hat{I}$, which, in turn, is derived from the background image \hat{I}_0 computed with the background slowness s_0 .

The perturbed image can be computed by the linearized-residual prestack-depth migration (Sava, 2003), and it is used in the wave-equation migration-velocity analysis (Biondi and Sava, 1999; Sava, 2004). Also, the perturbed image can be computed by the differential-semblance-optimization (DSO) operator (Symes and Carazzone, 1991), and it is used in the differential-semblance velocity optimization (DSVA) (Shen, 2004; Shen and Symes, 2008).

Under the ℓ_2 norm, the DSVA objective function J_{DSO} is

$$J_{\text{DSO}} = \frac{1}{2}\|\Delta\hat{I}\|_2 = \frac{1}{2}\|\mathbf{H}[\hat{I}_0]\|_2, \quad (12)$$

where \mathbf{H} is the DSO operator either in the subsurface-offset domain or in the angle domain. In the subsurface-offset domain, DSO penalizes energy at zero offset, by weighting the background image with the absolute value of the subsurface offset. In the angle domain, DSO penalizes flattening of events, by taking the derivative of the background image along the aperture angle.

Gradient-based optimization techniques, such as the nonlinear conjugate-gradient method, can be used in the optimization, to which the gradient must be explicitly computed. The gradient ∇J_{DSO} of the objective function with respect to the slowness \mathbf{s} is

$$\nabla J_{\text{DSO}} = \mathbf{T}'\mathbf{H}'\mathbf{H}I_0, \quad (13)$$

where $\mathbf{T} = \left. \frac{\partial I}{\partial s} \right|_{s=s_0}$ is the wave-equation tomographic operator (WETOM), which is composed of several operators and linearly maps the slowness perturbation Δs to the perturbed image.

WETOM has been evaluated in the source and receiver domain (Sava, 2004), in the shot-profile domain (Shen, 2004), and in the generalized-sources domain both in the data and in the image space (Tang et al., 2008). We discuss WETOM in the image-space generalized-sources domain, using 35 ISPEW modeled from the 12 reflectors of Figure 9, selected from the background image of Figure ??a.

In the areal-shot migration of image-space generalized wavefields, wavefields are downward continued with the following one-way wave equations:

$$\begin{cases} \left(\frac{\partial}{\partial z} + i\sqrt{\omega^2 s^2(\mathbf{x}) - |\mathbf{k}|^2} \right) \widehat{D}(\mathbf{x}, \mathbf{p}, \omega) = 0 \\ \widehat{D}(x, y, z = z_{min}, \mathbf{p}, \omega) = \widetilde{D}(x, y, z = z_{min}, \mathbf{p}, \omega) \end{cases}, \quad (14)$$

and

$$\begin{cases} \left(\frac{\partial}{\partial z} - i\sqrt{\omega^2 s^2(\mathbf{x}) - |\mathbf{k}|^2} \right) \widehat{U}(\mathbf{x}, \mathbf{p}, \omega) = 0 \\ \widehat{U}(x, y, z = z_{min}, \mathbf{p}, \omega) = \widetilde{U}(x, y, z = z_{min}, \mathbf{p}, \omega) \end{cases}, \quad (15)$$

where $\widehat{D}(\mathbf{x}, \mathbf{p}, \omega)$ is the image-space generalized downward wavefield for a single frequency, $\widehat{U}(\mathbf{x}, \mathbf{p}, \omega)$ is the image-space generalized upward wavefield for a single frequency; \mathbf{p} is the index of the areal shot, and $\widetilde{D}(x, y, z = z_{min}, \mathbf{p}, \omega)$ and $\widetilde{U}(x, y, z = z_{min}, \mathbf{p}, \omega)$ are the data synthesized with PERM using phase encoding or not, and collected at $z = z_{min}$, which denotes the top of a target zone. The PERM data serve as the boundary conditions of equations 14 and 15, respectively. Snapshots of image-space generalized background wavefields are shown in Figure 10.

The cross-correlation imaging condition produces the image $\hat{I}(\mathbf{x}, \mathbf{h})$ (Figure 11):

$$\hat{I}(\mathbf{x}, \mathbf{h}) = \sum_{\mathbf{p}} \sum_{\omega} \hat{D}^*(\mathbf{x} - \mathbf{h}, \mathbf{p}, \omega) \hat{U}(\mathbf{x} + \mathbf{h}, \mathbf{p}, \omega). \quad (16)$$

The perturbed image is derived by applying the product rule to equation 16, which gives

$$\begin{aligned} \Delta \hat{I}(\mathbf{x}, \mathbf{h}) = & \sum_{\mathbf{p}} \sum_{\omega} \Delta \hat{D}^*(\mathbf{x} - \mathbf{h}, \mathbf{p}, \omega) \hat{U}_0(\mathbf{x} + \mathbf{h}, \mathbf{p}, \omega) + \\ & \hat{D}_0^*(\mathbf{x} - \mathbf{h}, \mathbf{p}, \omega) \Delta \hat{U}(\mathbf{x} + \mathbf{h}, \mathbf{p}, \omega), \end{aligned} \quad (17)$$

where $\hat{D}_0(\mathbf{x} - \mathbf{h}, \mathbf{p}, \omega)$ and $\hat{U}_0(\mathbf{x} + \mathbf{h}, \mathbf{p}, \omega)$ are the image-space generalized background downward and upward wavefields computed with the background slowness; and $\Delta \hat{D}(\mathbf{x} - \mathbf{h}, \mathbf{p}, \omega)$ and $\Delta \hat{U}(\mathbf{x} + \mathbf{h}, \mathbf{p}, \omega)$ are the image-space generalized perturbed downward wavefield and the image-space generalized perturbed upward wavefield, respectively. These image-space generalized perturbed wavefields are the response to a slowness perturbation. The image-space generalized perturbed wavefields satisfy the following one-way wave equations linearized with respect to the slowness:

$$\left\{ \begin{array}{l} \left(\frac{\partial}{\partial z} + i\sqrt{\omega^2 s_0^2(\mathbf{x}) - |\mathbf{k}|^2} \right) \Delta \hat{D}(\mathbf{x}, \mathbf{p}, \omega) = \hat{D}_{SC}(\mathbf{x}, \mathbf{p}, \omega) \\ \Delta \hat{D}(x, y, z = z_{min}, \mathbf{p}, \omega) = 0 \end{array} \right. , \quad (18)$$

and

$$\left\{ \begin{array}{l} \left(\frac{\partial}{\partial z} + i\sqrt{\omega^2 s_0^2(\mathbf{x}) - |\mathbf{k}|^2} \right) \Delta \hat{U}(\mathbf{x}, \mathbf{p}, \omega) = \hat{U}_{SC}(\mathbf{x}, \mathbf{p}, \omega) \\ \Delta \hat{U}(x, y, z = z_{min}, \mathbf{p}, \omega) = 0 \end{array} \right. . \quad (19)$$

Snapshots of the image-space generalized perturbed wavefields are shown in Figure 12. Since the boundary conditions at z_{min} are null, no scattering occurs at depth levels shallower than z_{min} . The wavefields in the right-hand side of equations 18 and 19 are the image-space generalized scattered downward and upward wavefields, respectively, which result

from the interaction of the image-space generalized background wavefields with a slowness perturbation according to

$$\widehat{D}_{SC}(\mathbf{x}, \mathbf{p}, \omega) = \frac{i\omega\Delta s(\mathbf{x})}{\sqrt{1 - \frac{|\mathbf{k}|^2}{\omega^2 s_0^2(\mathbf{x})}}} \widehat{D}_0(\mathbf{x}, \mathbf{p}, \omega) \quad (20)$$

and

$$\widehat{U}_{SC}(\mathbf{x}, \mathbf{p}, \omega) = \frac{-i\omega\Delta s(\mathbf{x})}{\sqrt{1 - \frac{|\mathbf{k}|^2}{\omega^2 s_0^2(\mathbf{x})}}} \widehat{U}_0(\mathbf{x}, \mathbf{p}, \omega). \quad (21)$$

These wavefields are injected at every depth level during the recursive downward propagation of the perturbed wavefields. The image-space generalized perturbed source and receiver wavefields are used along with the precomputed image-space generalized background source and receiver wavefields in equation 17 to generate the perturbed image (Figure 13). The image-space generalized background source and receiver wavefields are obtained by recursively solving equations 14 and 15 using the background slowness.

The adjoint WETOM \mathbf{T}' is obtained by the following operations. First, the adjoint-imaging condition is applied to compute the image-space generalized perturbed source and receiver wavefields according to the following convolutions:

$$\begin{aligned} \Delta\widehat{D}(\mathbf{x}, \mathbf{p}, \omega) &= \sum_{\mathbf{h}} \Delta\widehat{I}(\mathbf{x}, \mathbf{h}) \widehat{U}_0(\mathbf{x} + \mathbf{h}, \mathbf{p}, \omega) \\ \Delta\widehat{U}(\mathbf{x}, \mathbf{p}, \omega) &= \sum_{\mathbf{h}} \Delta\widehat{I}(\mathbf{x}, \mathbf{h}) \widehat{D}_0(\mathbf{x} - \mathbf{h}, \mathbf{p}, \omega). \end{aligned} \quad (22)$$

The image-space generalized perturbed wavefields are upward propagated using the adjoint counterparts of equations 18 and 19. At every depth of their upward propagation, the image-space generalized perturbed source wavefield is cross-correlated with the image-space generalized scattered source wavefield, and the image-space generalized perturbed receiver wavefield is cross-correlated with the image-space generalized scattered receiver wavefield

to generate the slowness perturbation according to

$$\Delta\hat{s}(\mathbf{x}) = \sum_{\mathbf{p}} \sum_{\omega} \hat{D}_{SC}^*(\mathbf{x}, \mathbf{p}, \omega) \Delta\hat{D}(\mathbf{x}, \mathbf{p}, \omega) + \hat{U}_{SC}^*(\mathbf{x}, \mathbf{p}, \omega) \Delta\hat{U}(\mathbf{x}, \mathbf{p}, \omega). \quad (23)$$

The slowness perturbation for the Marmousi example computed in the image-space generalized sources domain using ISPEWs is shown in Figure 14.

When performing velocity optimization using DSVA, for instance, the perturbed image in equation 22 is computed with DSO at the beginning of every nonlinear iteration. DSO easily automates migration-velocity optimization. However, neither the phase nor the amplitudes of the DSO perturbed image are consistent with those of the perturbed image computed by the forward one-way ISWET operator. These differences prevent the use of linear conjugate-gradient methods, and therefore the objective function computed with DSO is typically minimized by nonlinear optimization methods.

The gradient of the wave-equation tomography objective function is sensitive to amplitude variations of the prestack image caused by uneven illumination. Since these amplitude variations are not related to velocity inaccuracy, we should ideally attenuate them using some sort of illumination compensation scheme (Valenciano et al., 2009; Tang, 2009). Instead, to prevent these amplitude variations we apply a B-spline smoothing to the gradient, which consists of representing the gradient as B-spline basis functions, using the adjoint operator \mathbf{B}' , and transforming it back to the Cartesian space, using the forward operator \mathbf{B} .

When using image-space generalized wavefields, a target-oriented strategy can be adopted if the velocity model is sufficiently accurate for shallower layers. A mask operator \mathbf{M} is applied to the gradient, zeroing out amplitudes in the accurate velocity region, preventing the

velocity model from being updated.

Since the gradient is not properly scaled, we normalize it with the diagonal operator \mathbf{F} , which is the smallest value of the initial slowness divided by the maximum absolute value of the gradient. To improve and sometimes guarantee convergence, we would like to limit the velocity update from one iteration with respect to its previous values. In other words, we would like the new velocity to vary within a range defined by a percentage of the velocity from the previous iteration. This can be implemented by applying to the gradient either a nonlinear (since it depends on the velocity) diagonal operator, or a diagonal operator \mathbf{W} linearized around the initial velocity. Therefore, the final gradient is

$$\nabla J_{DSO} = \mathbf{W}\mathbf{F}\mathbf{M}\mathbf{B}\mathbf{B}'\mathbf{T}'\Big|_{s=s_0} \mathbf{H}'\mathbf{H}\tilde{\mathbf{I}}\Big|_{s=s_0}, \quad (24)$$

In the next section, we use the operators described above to smooth and scale the gradient in a velocity-optimization problem for a 3D field-data example.

3D FIELD-DATA EXAMPLE

3D FIELD-DATA EXAMPLE

The 3D North Sea dataset spans over an area of approximately 55 km², with 13.5 km in-lines and 4 km cross-lines. It was acquired using dual sources at intervals of 25 m in the in-line direction and 50 m in the cross-line direction, with three cables with 100 m separation and a maximum offset 3600 m. The limited cross-line offsets (Figure 15d) resulting from this acquisition configuration impose limitations in the azimuthal distribution, as can be seen in Figure 15a and 15b. The overall in-line-offset distribution is quite regular (Figure 15c). However, the offset distribution is spatially quite irregular. The fold of coverage computed

for a grid cell of 25 X 25 m for different offset ranges is shown in Figure 16. The acquisition footprint is evident, with a wide low-fold region occurring for in-lines around 4000 m in the y direction.

To mitigate the offset irregularity, considering the limited azimuthal distribution, Clapp (2005, 2006) applies least-squares 3D-data regularization using offset volumes transformed to a common offset via AMO (Biondi et al., 1998). In spite of the good imaging results, the amplitude variation caused by the offset irregularity, although diminished, still persists as can be seen in Figure 17. It shows time slices at 2.8 s through the trace envelope for different offset cubes taken from the regularized data provided by Clapp.

Even though the fold irregularity (Figure 16) and amplitude imbalance (Figure 17) are in the data-space, we will see later that they will be evident in the amplitudes of the gradient of the objective function at approximately the same spatial position.

The velocity model provided along with the data (Figure 18), herein called the original velocity model, presents a general layered structure with an overhanging salt dome connected to a deeper layer with the same velocity as that of the salt dome. In Figure 18, the maximum velocity is 4820 m/s. The final velocity model I derive shows remarkable differences when compared to the original velocity model, especially in the salt body shape.

I start ISWET with an initial velocity model derived from the original velocity model. Initially, the sediment velocity above the chalk layer was refined using residual prestack depth-migration scans. Then, I interpreted the top of chalk on an image migrated with this new velocity. Below the top of chalk, velocity was heavily smoothed using a 5000 m wide 2D median smoother. In addition, to increase the inaccuracy of the initial velocity model,

velocity was scaled down by a factor of 0.9 (Figure 19). In Figure 19, the initial velocity model is displayed with the same color scale as that of Figure 18 and the maximum velocity is 4100 m/s. A layer-stripping approach was used to define the velocity for the chalk layer, considering a sufficiently accurate velocity for the sediments above. Then, the top salt was interpreted, and a salt flooding procedure enabled the interpretation of the base of salt. The interpretation of the base of salt can be considered the main source of uncertainty of the 3D-field data example, since no previous geological information was available. Finally, a group of reflectors below the salt is used to define the velocity structure for the deeper part.

All the computations were carried out on computer nodes of the Stanford Center for Computational Earth & Environmental Science (CEES). Thirty nodes of Dual Nehalem 5520 with 24Gb RAM were used, accounting to 240 CPUs. To generate 30 pairs of 3D ISPEWs, using 196 frequencies, it took 10 minutes. On average, each iteration of the velocity optimization, consisting of one function evaluation, the gradient computation, and two additional function evaluations for the line search, took approximately two hours.

IMPROVING VELOCITY ABOVE THE CHALK

When defining the depth-migration velocity model, it is very important that velocity in the shallow layers is sufficiently accurate, so that velocity errors are not propagated to deeper layers. A first version of the initial velocity Figure 20 was generated in a similar way as that for Figure 19, except that the velocity above the top of the chalk is the same as the original velocity. Migration with this version of the initial velocity revealed slight velocity inaccuracies for the sediment layer above the chalk, evidenced by residual moveout in the SODCIGs (Figure 21). The section on the top is the zero-subsurface-offset section, and the

panels at the bottom are SODCIGs at the position corresponding to their x coordinates. Notice the shallow events curving down in the SODCIGs, especially for x coordinates below 6000 m. The strong reflector, which is flat at depths of 1500 m on the left and 1300 m on the right, and curved in the middle of the figure, is the top of chalk. It also presents strong curvature. The residual moveout of these gathers was evaluated with residual-prestack-depth migration velocity analysis (Sava, 2003), in which a residual moveout parameter was interpreted. Since the velocity structure is approximately one-dimensional and the residual-moveout parameter is local, I performed one run of a simple vertical velocity update similar to Deregowski's velocity update (Deregowski, 1990).

The new velocity model satisfactorily improved the focusing of the image, as can be seen in Figure 22. Notice how both the shallow reflectors and the top of chalk are much better focused around zero-subsurface offset. Also, since the interval velocities increased, the top of chalk is shifted down. The maximum frequency used to compute images of Figures 21 and 22 is 60 Hz. For velocity optimization and the following common-azimuth migration images, the maximum frequency is 42 Hz.

SOLVING FOR THE CHALK LAYER VELOCITY

Generating 3D ISPEWs for the base of chalk

After improving the accuracy of the initial velocity model for the shallower sediment layers, as previously discussed, common-azimuth migration (CAM) with this initial velocity (Figure 19) produced the images in Figure 23, which shows the volume for the zero subsurface offset, and Figure 24, which shows the zero subsurface offset on the left, and ADCIGs on the right for in-line 3180. The effects of migrating with a too low velocity are evidenced by poorly

collapsed diffractions close to the salt flank, poorly imaged faults, and reflectors curving up in the ADCIGs.

For the modeling of ISPEWs, in-line and cross-line intervals of the CAM image were interpolated from 20 m to 30 m, which are the in-line and cross-line intervals used for optimizing the migration velocity. The base of chalk was interpreted in the 3D pre-stack volume, using the latest version of the hypercube viewer (Clapp et al., 2008).

After migration, the wavelet is velocity- and dip-dependent (Tygel et al., 1994). Although simple in 2D, implementing 3D windowing based on the dip- and velocity-dependent wavelet stretching can be cumbersome. Instead, I use a simpler procedure that yields a mask operator to window the reflector. First, I use the pre-stack interpretation to vertically window the target reflectors. Then, for each windowed subsurface-offset cube, I compute the tridimensional envelope with the same smoothing parameter in all directions, which simulates the dip dependency. The amplitudes are clipped to one, based on a threshold value. Amplitude variations are compensated for by applying an RMS gain prior to the computation of the envelope. The mask operator is shown in Figure 25 for the zero subsurface offset (Figure 25a) and for the in-line 3520 (Figure 25b), in which a subsurface-offset gather is shown on the right.

We extract the signed square root of the windowed pre-stack image to minimize the influence of the squaring of the wavelet on the gradient computation, as discussed in Chapter ??.

As shown in Chapter ??, the CAM initial conditions can be continuously sampled in the cross-line direction, because no cross-line offset is computed; this reduces by at least one order of magnitude the number of image-space generalized wavefields to be synthesized.

For the base of chalk, we modeled only 30 3D ISPEWs, which are collected at 600 m depth. Using 30 CEES nodes with 8 CPUs each, the modeling takes approximately 10 minutes. A pair of 3D-ISPEW gathers is shown in Figure 26. Since the number of subsurface offsets that will be used during ISWET is 25 and the spatial sampling in the x direction of 30 SODCIGs is used to model the 3D ISPEWs, crosstalk is expected to be strongly attenuated during imaging in ISWET.

Velocity optimization

A nonlinear conjugate-gradient solver is used for the velocity optimization. Velocity update is constrained to a maximum of 10% variation between iterations. All the wavefield propagation is performed between the depth at which the 30 3D ISPEWs were collected (600 m) and the maximum depth (3300 m). Velocity is updated up to the top of the chalk layer.

The amplitude variations are more pronounced in 3D than in 2D because of the acquisition footprint. To illustrate the amplitude variation problem, we compute the slowness perturbation without applying smoothing, and without extracting the signed square root from the initial conditions, to model 30 pairs of ISPEWs (Figure 27). In this case, the amplitude variation due to acquisition is even more pronounced. The acquisition footprint is clear, specially around the y coordinate 4000 m, which is a region with low-fold of coverage (Figure 16). If we extract the signed square root of the initial conditions for the modeling, or equivalently the signed fourth root of the gradient, the DSO slowness perturbation presents smaller amplitude variations (Figure 28).

The gradient of the objective function must be smooth to yield velocity updates consistent with the Born approximation, as discussed in Chapter ???. We apply a B-spline

smoothing with node intervals of 420 X 420 X 160 m in the in-line, cross-line and depth directions, respectively. Applying B-spline smoothing on the DSO slowness perturbation of Figure 28 mitigates the amplitude-variation problems and yields consistent slowness perturbations (Figure 29).

Two runs of ISWET were necessary to define the velocity model for the chalk layer. In the first, we used the 30 pairs of ISPEWs whose modeling was described in the previous subsection. We used two function evaluations in the line search. After seven iterations, optimization stopped because the variation of the objective function was smaller than 0.1%. Figure 30 shows the evolution of the objective function.

The optimized velocity for the first run of ISWET is shown in Figure 33. As expected, the migration velocity increased compared to the initial velocity of Figure 19. The initial background image and the background image of the seventh iteration can be seen in Figures 31 and 32, respectively. On the left is the zero-subsurface-offset section, and on the right are the SODCIGs. Overall, the focusing around the zero subsurface offset improved. However, close to the salt flanks, SODCIGs still show events curving down, indicating velocity inaccuracy.

The velocity inaccuracy close to the salt flanks motivated a second run of ISWET for the base of chalk. Again, 30 pairs of ISPEWs were modeled, but from initial images limited to approximately 2 km around the salt body. By doing this, we explore the localized nature of these wavefields, as discussed in Chapter ??, so that this second run is targeted for updating the velocity close to the salt flanks. The optimized velocity for the second run of ISWET is shown in Figure 34. Migration velocity further increased compared to the optimized velocity of the first run (Figure 33). CAM using this optimized velocity is shown in Figure

35, which shows the volume for the zero subsurface offset, and Figure 36, which shows the zero subsurface offset on the top, and ADCIGs at the bottom for in-line 3180. Compare these figures with Figures 23 and 24, respectively. The optimized velocity model allowed imaging of a complex fault system on the right of the salt body, collapsing diffractions from the salt flank, and flattening reflectors in the ADCIGs.

SALT FLOODING

Once a sufficiently accurate velocity for the chalk layer had been defined, salt flooding was used to delineate the salt body. The top salt was interpreted, and below the velocity was replaced by a constant value of 4500 m/s (Figure 37). The picking of the top of salt is a source of uncertainty for defining the velocity model below, since it is difficult to manually interpret all the high-wavenumber components of the irregular top of salt. A solution to this problem should use automatic procedures to identify the top of salt (Lomask, 2006; Halpert, 2010).

The CAM migrated image (Figure 38) computed with the velocity of Figure 37 was sufficiently focused to support the interpretation of the base of the salt. As can be seen in Figure 38, the lack of a continuous reflector makes the interpretation of the base of salt challenging. Insufficient illumination due to the limited azimuthal coverage and irregular shape of the salt body caused the base of salt to be discontinuous. In this situation, prior geological information would be extremely helpful to constrain the interpretation. The lack thereof is another source of uncertainty for defining the velocity model below the salt.

After the base of salt was interpreted, the velocity was edited again (Figure 39), so that the salt velocity was confined within the salt body and the initial velocity was inserted below

the salt and the chalk layer. With this new velocity model, another run of CAM generated the image in Figure 40 from which deeper reflectors are used to model new ISPEWs to be used in ISWET for deeper layers.

SOLVING FOR SUB-SALT VELOCITIES

On the prestack image of Figure 41, resulting from CAM with the sufficiently accurate velocity model for the chalk layer and the salt body, seven reflectors were interpreted (Figure 42) to be used as the initial conditions for the modeling of 3D ISPEWs for defining sub-salt velocities. Again, 30 pairs of 3D-source and -receiver ISPEWs were generated. These wavefields were collected at a depth of 1650 m, which is the minimum depth used in the velocity optimization. The prestack image used as the initial conditions for the modeling has 33 in-line subsurface offsets with 30 m intervals and a maximum offset 480 m. The CMP interval in the x and y directions is 30 m.

The initial velocity used in the sub-salt velocity optimization is shown in Figure 39. The shallower limit for velocity updating is represented by the base of chalk and base of salt, and the deeper limit is 4800 m. The interval between B-spline nodes is 1050 m in the x and y directions and 150 m in the z direction. A maximum of 5% local velocity variation is allowed between iterations, and two function evaluations are performed in the line search.

The evolution of the objective function normalized by its initial value is shown in Figure 43. Velocity optimization stopped after 7 iterations because the update of the objective function was smaller than 0.1%. The final objective function dropped 10%. This decrease is small compared to the 40% decrease of the objective function for the velocity optimization of the base of chalk. For the chalk case, only crosstalk from different SODCIGs was generated

because only one reflector was used to generate the 3D ISPEWs. For the sub-salt case, in addition to the crosstalk from different SODCIGs, reflector crosstalk was generated since seven reflectors were used as the initial conditions. Hence, the amount of background dispersed crosstalk is greater in the sub-salt case than in the chalk case, explaining the smaller decrease of the objective function in the sub-salt velocity optimization.

The evolution of the velocity model through iterations is shown in Figure 44.

CAM with the optimized velocity model can be seen in Figure 45. For comparison, CAM with the initial velocity model and CAM with the original velocity model are shown in Figures 46 and 47. When compared with the results using the initial velocity model, the improvements obtained with the optimized velocity model are clear: flatter angle gathers, better focusing of the reflectors, and imaging of the faults. The improvements compared to the original (unmodified) velocity model are also clear: better focusing of reflectors and slightly flatter angle gathers below the salt as well as close to its flanks.

Next, I show more systematic comparisons of the results computed with the initial, original and the final velocity models.

COMPARISONS

Here, I show three comparisons between the CAM images obtained with the initial, with the original, and with the final velocity models, for different in-lines and cross-lines. The images are displayed as vertical slices through the migrated cube and show the zero subsurface offset. The left panel of each figure shows the in-line, and the right panel shows the cross-line.

Figure captions explain the differences highlighted by ovals. Overall, the final images

present better quality than do the initial and original images, expressed by better focusing and continuity of reflectors in the chalk layer as well as in the sub-salt region. Certainly, the final image would ease interpretation and understanding of geological and structural history, adding more value to seismic information in an exploratory study.

CONCLUSIONS

The 3D-field data North Sea turned out to be a very challenging dataset. The challenges were represented by the narrow azimuth configuration and irregular fold of coverage, causing incomplete and irregular illumination of the reflectors. Also, the irregular salt body and intense faulting were difficult targets to delineate and image. The problems with the illumination, evidenced by amplitude irregularity of the gradient of the objective function, were mitigated by properly scaling the prestack image used to model the 3D ISPEWs and the gradient of the objective function, and by smoothing the gradient of the objective function.

Using 3D ISPEWs has proved to greatly accelerate 3D ISWET, due to the small number of wavefields needed to satisfactorily describe the kinematics of the prestack image and the fact that they are computed in a target-oriented manner. These synthesized wavefields made it possible to solve 3D ISWET in an academic environment with limited computational resources. Considering the computational resources available in the industry, using 3D ISPEWs can turn 3D ISWET an interactive process, which can yield more reliable solutions.

Solving for migration velocity in a target-oriented manner with wave-equation methods allows updating the velocity model not only within a limited depth range, but also within a limited lateral extent. This is achieved by selecting a specific portion of a reflector or group of reflectors that still present residual moveout. This feature was demonstrated when

updating the velocity model in the vicinity of the salt body, using only a small portion of the reflector corresponding to the base of chalk close to the salt.

Besides the computational gain, 3D ISPEWs were able to provide reliable velocity updates. Using the final velocity model produces a CAM image with quality superior to that obtained with the initial velocity model, as expected. Moreover, the image computed with the final velocity model is more accurate than that computed with the original velocity model, with better focusing and continuity of the sub-salt reflectors and better fault imaging.

ACKNOWLEDGMENTS

I would like to thank Bob Clapp for making available the common-azimuth migration code and for continuously improving SEP's 3D-interpretation and visualization capability. I am indebted to Dennis Michael, manager of the High Productivity Technical Computing (HTPC) initiative hosted by CEES, for his continuous support.

REFERENCES

- Biondi, B., 2006, Prestack exploding-reflectors modeling for migration velocity analysis: 76th Ann. Internat. Mtg., Expanded Abstracts, 3056–3060, Soc. of Expl. Geophys.
- Biondi, B., S. Fomel, and N. Chemingui, 1998, Azimuth moveout for 3-D prestack imaging: *Geophysics*, **63**, 574–588.
- Biondi, B. and P. Sava, 1999, Wave-equation migration velocity analysis: SEG Technical Program Expanded Abstracts, **18**, 1723–1726.
- Biondi, B. and W. W. Symes, 2004, Angle-domain common-image gathers for migration velocity analysis by wavefield-continuation imaging: *Geophysics*, **69**, 1283–1298.
- Clapp, R., 2005, AMO inversion to a common azimuth dataset: **SEP-123**, 91–101.
- Clapp, R. G., 2006, AMO inversion to a common azimuth dataset: SEG Technical Program Expanded Abstracts, **25**, 2097–2101.
- Clapp, R. G., D. M. Chen, and S. Luo, 2008, Hypercube viewer: **SEP-134**, 179–192.
- Deregowski, S., 1990, Common offset migrations and velocity analysis: *First Break*, **8**, 224–234.
- Duquet, B. and P. Lailly, 2006, Efficient 3D wave-equation migration using virtual planar sources: *Geophysics*, **71**, S185–S197.
- Guerra, C., 2010, Migration-velocity analysis using image-space generalized wavefields, *in* Ph.D. thesis, Stanford University.
- Guerra, C. and B. Biondi, 2008, Phase encoding with gold codes for wave-equation migration: **SEP-136**, 23–42.
- Halpert, A., 2010, A new method for more efficient seismic image segmentation: **SEP-140**, 213–228.
- Liu, F., D. W. Hanson, N. D. Whitmore, R. S. Day, and R. H. Stolt, 2006, Toward a unified

- analysis for source plane-wave migration: *Geophysics*, **71**, 129–139.
- Lomask, J., 2006, Seismic volumetric flattening and segmentation, *in* Ph.D. thesis, Stanford University.
- Rickett, J. E. and P. C. Sava, 2002, Offset and angle-domain common image-point gathers for shot-profile migration: *Geophysics*, **67**, 883–889.
- Romero, L., D. Ghiglia, C. Ober, and S. Morton, 2000, Phase encoding of shot records in prestack migration: *Geophysics*, **65**, 426–436.
- Sava, P., 2003, Prestack residual migration in frequency domain: *Geophysics*, **68**, 634–640.
- , 2004, Migration and velocity analysis by wavefield extrapolation, *in* Ph.D. thesis, Stanford University.
- Sava, P. and S. Fomel, 2006, Time-shift imaging condition in seismic migration: *Geophysics*, **71**, S209–S217.
- Schultz, P. S. and J. Claerbout, 1978, Velocity estimation and downward continuation by wavefront synthesis: *Geophysics*, **43**, 691–714.
- Shen, P., 2004, Wave-equation Migration Velocity Analysis by Differential Semblance Optimization: PhD thesis, Rice University.
- Shen, P. and W. W. Symes, 2008, Automatic velocity analysis via shot profile migration: *Geophysics*, **73**, VE49–VE59.
- Sun, P., S. Zhang, and F. Liu, 2002, Prestack migration of areal shot records with phase encoding: 72nd Ann. Internat. Mtg, Soc. Expl. Geophys., Expanded Abstracts, 1172–1175.
- Symes, W. W. and J. J. Carazzone, 1991, Velocity inversion by differential semblance optimization: *Geophysics*, **56**, 654–663.
- Tang, Y., 2009, Target-oriented wave-equation least-squares migration/inversion with

- phase-encoded hessian: *Geophysics*, **74**, WCA95–WCA107.
- Tang, Y., C. Guerra, and B. Biondi, 2008, Image-space wave-equation tomography in the generalized source domain: **SEP-136**, 1–23.
- Tygel, M., J. Schleicher, and P. Hubral, 1994, Pulse distortion in depth migration: *Geophysics*, **59**, 1561–1569.
- Valenciano, A. A., B. L. Biondi, and R. G. Clapp, 2009, Imaging by target-oriented wave-equation inversion: *Geophysics*, **74**, WCA109–WCA120.
- Whitmore, N. D., 1995, An imaging hierarchy for common angle plane wave seismograms, *in* Ph.D. thesis, University of Tulsa.
- Yang, T. and P. Sava, 2009, Wave-equation migration velocity analysis using extended images: *SEG Technical Program Expanded Abstracts*, **28**, 3715–3719.

LIST OF FIGURES

1 Geometry for the computation of SODCIGs. Source, receiver and image points are labeled with S, R and I, respectively. The subscript hx corresponds to subsurface offsets computed with horizontal shift. The subscript hg corresponds to subsurface offsets computed by shifting along the apparent geological dip α . a) Underestimated velocity, and b) overestimated velocity. Modified from Biondi and Symes (2004).

2 Velocity models for the Marmousi example: a) Smooth velocity model used to model the Born data. b) Background velocity model used to migrate the Born data, and to model and migrate PERM data.

3 a) Pre-stack image computed with the background velocity model. b) Selected reflectors from the background image to perform modeling of wavefields.

4 PERM wavefields for the Marmousi example: a) Upward wavefield. b) Downward wavefield.

5 ISPEW for the Marmousi example: a) Upward wavefield. b) Downward wavefield.

6 Pre-stack image computed with PERM wavefields and background velocity model using: a) the conventional imaging condition (equation ??), and b) the time-windowed imaging condition (equation 9). Reflector crosstalk is avoided when reflectors are sufficiently separated. However, some residual crosstalk is still present (RC). Notice the phase difference of the PERM image due to the squaring of the wavelet when compared to the windowed reflectors of Figure 3b.

7 Pre-stack images computed with: a) Four random realizations of ISPEWs, and b) a single random realization.

8 ADCIGs (top) and ρ -panels (bottom) corresponding to images computed by: a) Shot-profile migration of 360 shot gathers, b) areal-shot migration of 35 PERM wave-

fields using the time-windowed imaging condition, c) areal-shot migration of 44 ISPEWs corresponding to four random realizations, and d) areal-shot migration of 11 ISPEWs corresponding to a single random realization. The moveout information is basically the same.

9 Selected reflectors used to model 35 pairs of ISPEW.

10 Snapshots of image-space generalized background wavefields: a) downward, and b) upward wavefields.

11 Background image computed with the image-space generalized background wavefields of Figure 10.

12 Snapshots of image-space generalized perturbed wavefields: a) source, and b) receiver.

13 Perturbed image computed with equation 17.

14 Slowness perturbation from back-projected image perturbations computed with 35 ISPEWs.

15 a) Offset – azimuth cross-plot, b) azimuth histogram, c) in-line offset histogram, and d) cross-line offset histogram.

16 Fold of coverage plots: a) full offset, b) 0 – 1200 m offset, c) 1200 – 2400 m offset, and d) 2400 – 3600 m offset.

17 Time slices through the trace envelope for different offset cubes from the regularized data: a) offset 200m, b) offset 1200 m, c) offset 2400 m, and d) offset 3000 m.

18 Slices through the IFP velocity model.

19 Slices through the initial velocity model used in 3D-ISWET.

20 Slices through an initial velocity model generated with the same procedures as that for Figure 19, except for the velocity above the chalk, which is the original velocity.

21 Image computed with the velocity model of Figure 20. The top panel is the zero-

subsurface offset section and the panel at the bottom are the SODCIGs.

22 Image computed with the velocity model of Figure 19. The left panel is the zero-subsurface offset section and the panels on the right are the SODCIGs. Compare with Figure 21.

23 Slices through the CAM image with the initial velocity model of Figure 19. Notice poorly collapsed diffractions close to the salt flank (A and D), and poorly imaged faults (B and C) caused by migrating with an inaccurate velocity.

24 In-line 3180 of the CAM image with the initial velocity model of Figure 19. On the left is the zero-subsurface offset section, and on the right ADCIGs. Notice the strong residual moveout on the ADCIGs. The continuous blue line is the top of chalk, and the dashed blue line is the base of chalk.

25 Slices through the prestack-mask operator to select the base of chalk, showing: a) the zero subsurface offset, and b) the in-line 3520.

26 A pair of 3D source (a) and receiver (b) ISPEWs computed for the base of chalk.

27 Slowness perturbation without smoothing and without extracting the signed square root from the initial conditions for the modeling of 30 pairs of ISPEWs.

28 Slowness perturbation without smoothing and extracting the signed fourth root of the gradient.

29 Slowness perturbation after B-spline smoothing the slowness perturbation of Figure 28.

30 Evolution of the DVSA objective function for the first run of ISWET for the base of chalk.

31 In-line 3520 of the initial background image of the first run of ISWET for the base of chalk.

32 In-line 3520 of the background image computed with the optimized velocity model of the first run of ISWET for the base of chalk.

33 Slices through the optimized velocity from the first run of ISWET for the base of chalk. The dashed white line approximately represents the base of chalk.

34 Slices through the optimized velocity from the second run of ISWET for the base of chalk. The dashed white line approximately represents the base of chalk.

35 Slices through the CAM image with the optimized velocity model of Figure 34. Notice the imaging of a big fault close to the salt flank (A), and the focusing of a complex fault system (B, C, and D).

36 In-line 3180 of the CAM image with the optimized velocity model of Figure 34. On the left is the zero-subsurface offset section, and on the right ADCIGs. Notice flatter reflectors in the ADCIGs compared to those in Figure 24. The continuous blue line is the top of chalk, and the dashed blue line it the base of chalk.

37 Slices through the velocity volume after salt flooding. The dashed white line approximately represents the base of chalk.

38 Slices through the CAM migrated image computed with the salt flooding velocity model of Figure 37.

39 Slices through the velocity volume after interpretation of the base of salt.

40 Slices through the CAM migrated image computed with the velocity model of Figure 39.

41 Slices through the prestack image computed with the migration velocity of Figure 39: a) the zero subsurface offset, and b) the in-line 3520.

42 Slices through the windowed prestack image, showing the selected reflectors for the modeling of 30 3D ISPEWs to be used in the sub-salt velocity optimization: a) the zero

subsurface offset, and b) the in-line 3520.

43 Evolution of the DVSA objective function of the sub-salt velocity optimization.

44 Slices through velocity models for: a) first iteration, b) third iteration, c) fifth iteration, and d) seventh iteration.

45 In-line 4060 of the CAM image with the final velocity model after optimization for the chalk layer, salt flooding, and sub-salt velocity optimization. On the top is the zero-subsurface offset section, and at the bottom ADCIGs.

46 In-line 4060 of the CAM image with the initial velocity model. On the top is the zero-subsurface offset section, and at the bottom ADCIGs.

47 In-line 4060 of the CAM image with the original velocity model. On the top is the zero-subsurface offset section, and at the bottom ADCIGs.

48 On the left panel is the in-line 3320 and on the right panel is the cross-line 5220 of the CAM images obtained with: a) the initial velocity model, b) the original velocity model, and c) the final velocity model after optimization for the chalk layer, salt flooding, and sub-salt velocity optimization. The oval in the in-line of the final image show better focusing and continuity for the sub-salt reflectors as well as for the salt flank. Besides focusing and continuity, the oval in the cross-line of the final image show unstructured sub-salt reflectors not pulled up by velocity errors.

49 On the left panel is the in-line 3680 and on the right panel is the cross-line 6880 of the CAM images obtained with: a) the initial velocity model, b) the original velocity model, and c) the final velocity model after optimization for the chalk layer, salt flooding, and sub-salt velocity optimization. The oval in the in-line of the final image show better focusing and continuity for the sub-salt reflectors. Besides focusing and continuity, the oval in the cross-line of the final image show unstructured sub-salt reflectors not pulled up by

velocity errors.

50 On the left panel is the in-line 4060 and on the right panel is the cross-line 9400 of the CAM images obtained with: a) the initial velocity model, b) the original velocity model, and c) the final velocity model after optimization for the chalk layer, salt flooding, and sub-salt velocity optimization. The oval in the in-line of the final image show better focusing and continuity for the sub-salt reflectors. In the cross-line, the upper oval of the final image show better definition of subtle faults in the chalk layer, the lower oval highlights better continuity of the reflectors, and the arrow labeled "F" indicates better fault imaging not clear in the initial and original images.

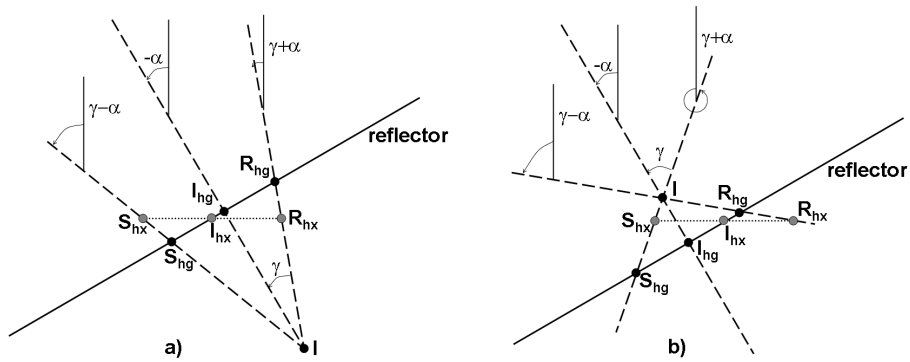


Figure 1: Geometry for the computation of SODCIGs. Source, receiver and image points are labeled with S, R and I, respectively. The subscript hx corresponds to subsurface offsets computed with horizontal shift. The subscript hg corresponds to subsurface offsets computed by shifting along the apparent geological dip α . a) Underestimated velocity, and b) overestimated velocity. Modified from Biondi and Symes (2004).

Guerra and Biondi –

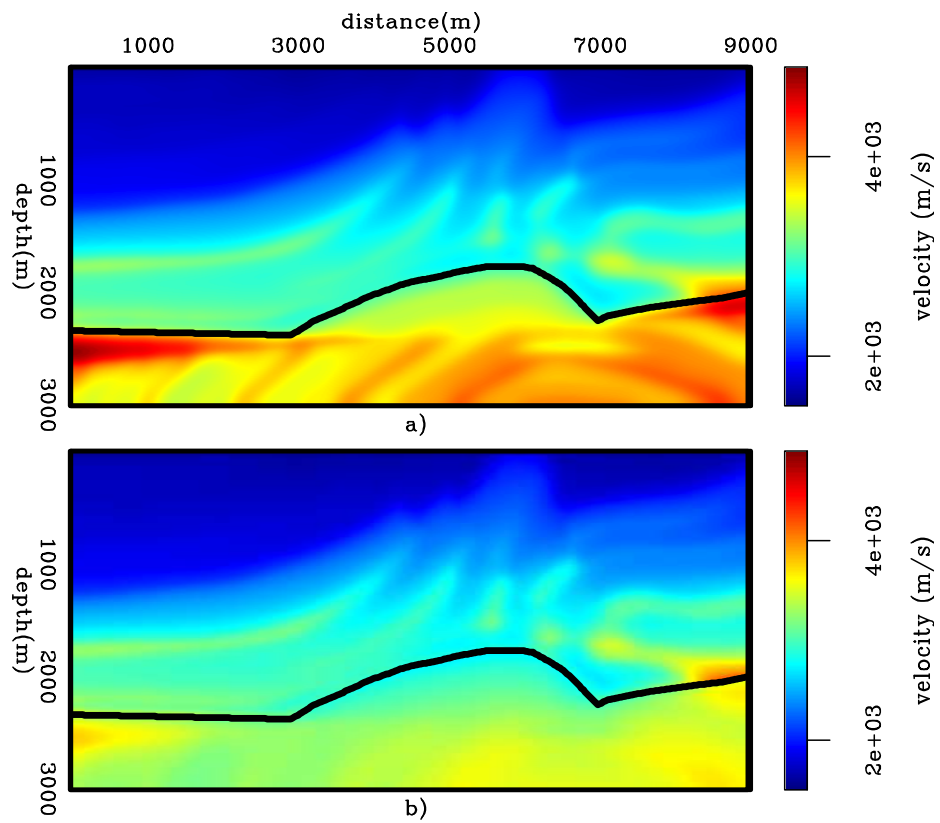


Figure 2: Velocity models for the Marmousi example: a) Smooth velocity model used to model the Born data. b) Background velocity model used to migrate the Born data, and to model and migrate PERM data.

Guerra and Biondi –

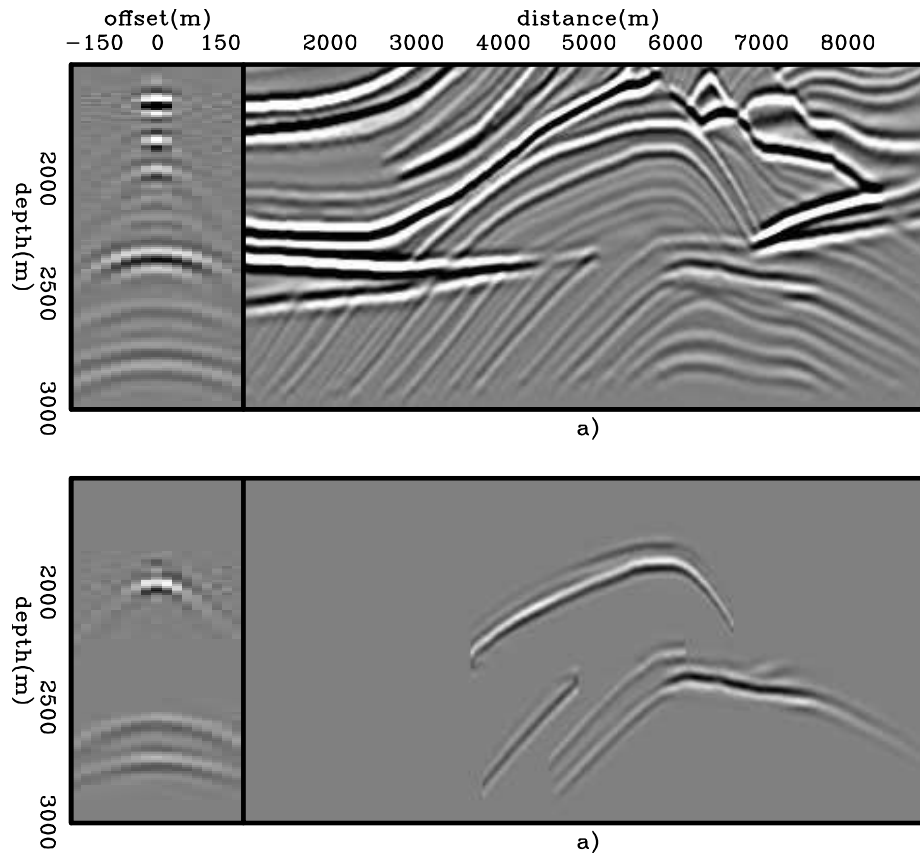


Figure 3: a) Pre-stack image computed with the background velocity model. b) Selected reflectors from the background image to perform modeling of wavefields.

Guerra and Biondi –

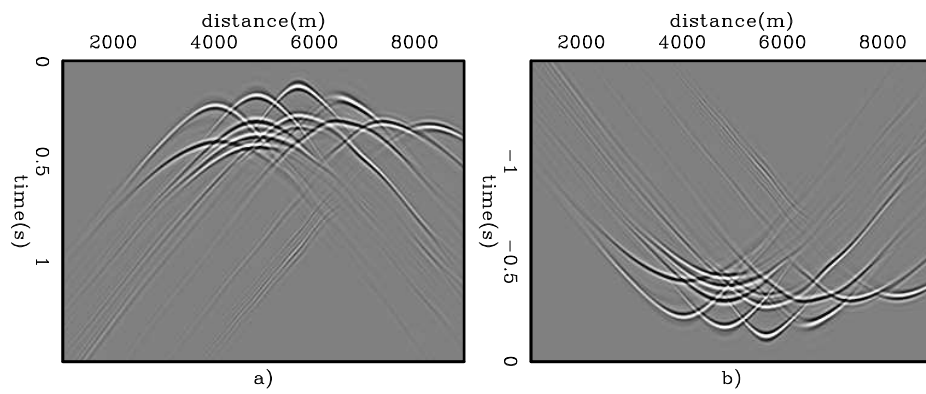


Figure 4: PERM wavefields for the Marmousi example: a) Upward wavefield. b) Downward wavefield.

Guerra and Biondi –

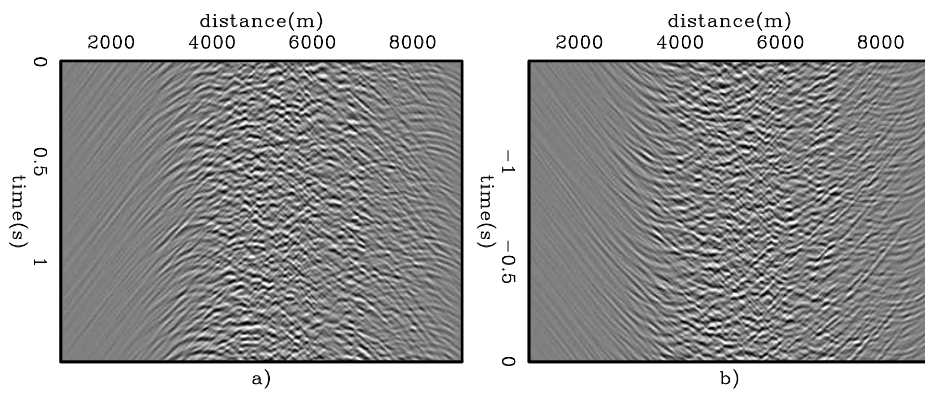


Figure 5: ISPEW for the Marmousi example: a) Upward wavefield. b) Downward wavefield.

Guerra and Biondi –

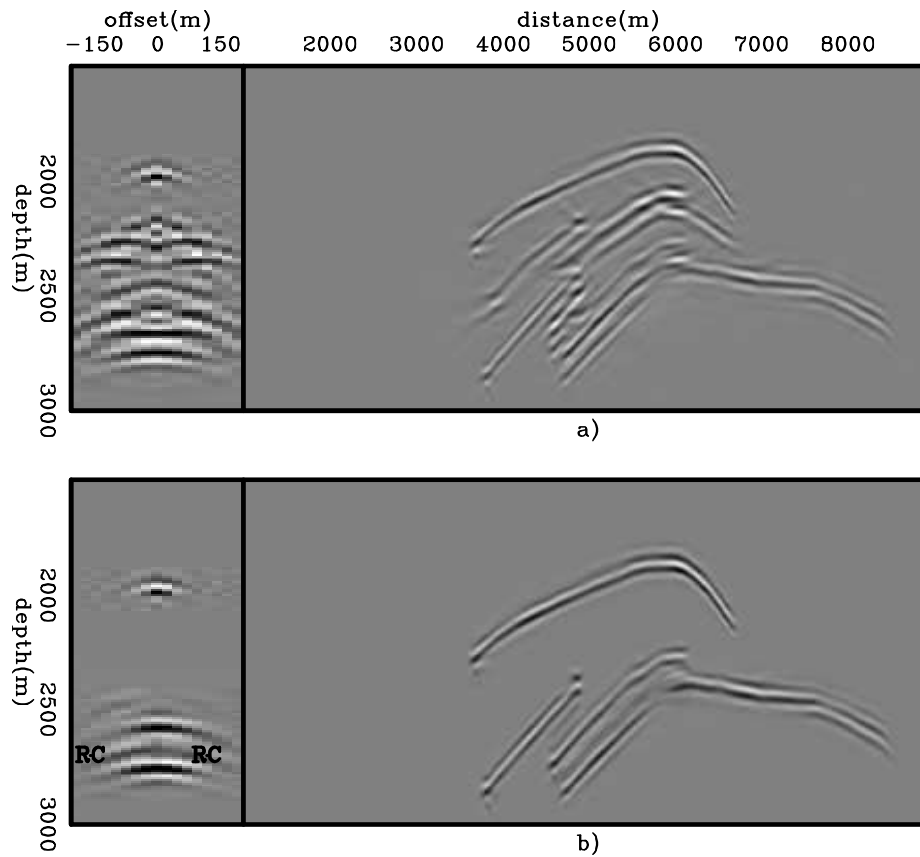


Figure 6: Pre-stack image computed with PERM wavefields and background velocity model using: a) the conventional imaging condition (equation ??), and b) the time-windowed imaging condition (equation 9). Reflector crosstalk is avoided when reflectors are sufficiently separated. However, some residual crosstalk is still present (RC). Notice the phase difference of the PERM image due to the squaring of the wavelet when compared to the windowed reflectors of Figure 3b.

Guerra and Biondi –

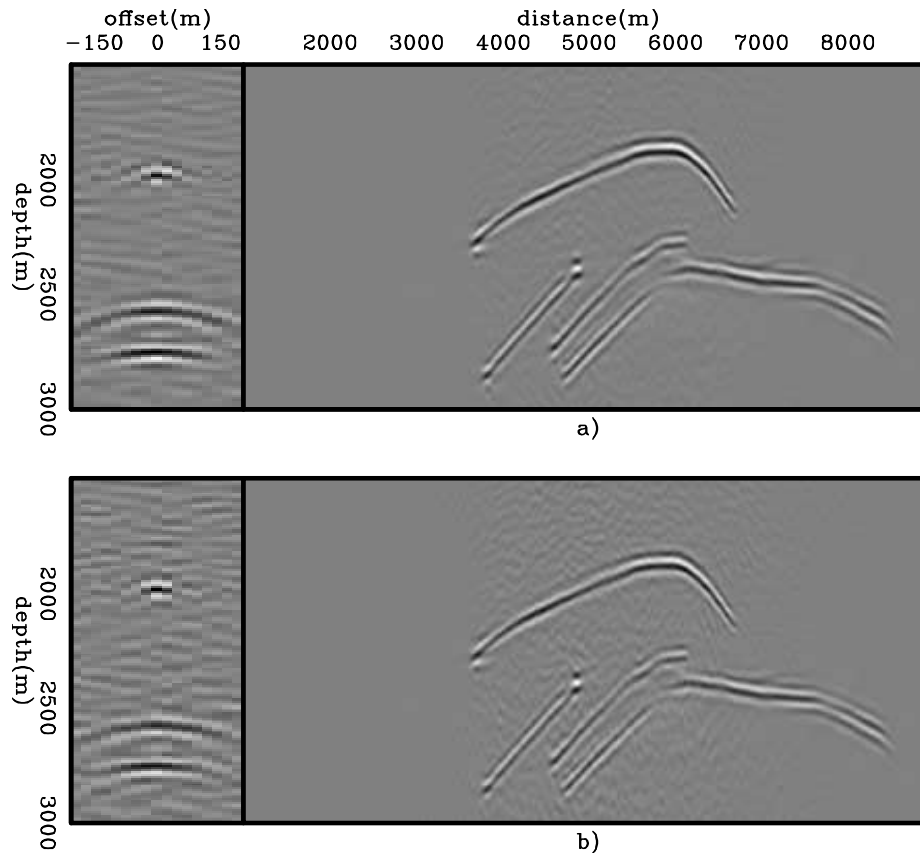


Figure 7: Pre-stack images computed with: a) Four random realizations of ISPEWs, and b) a single random realization.

Guerra and Biondi –

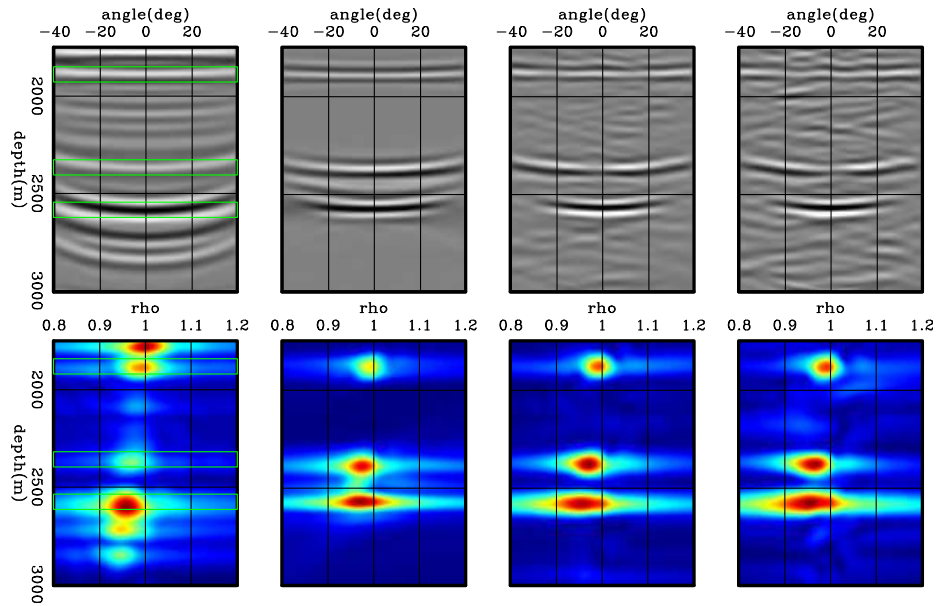


Figure 8: ADCIGs (top) and ρ -panels (bottom) corresponding to images computed by: a) Shot-profile migration of 360 shot gathers, b) areal-shot migration of 35 PERM wavefields using the time-windowed imaging condition, c) areal-shot migration of 44 ISPEWs corresponding to four random realizations, and d) areal-shot migration of 11 ISPEWs corresponding to a single random realization. The moveout information is basically the same.

Guerra and Biondi –

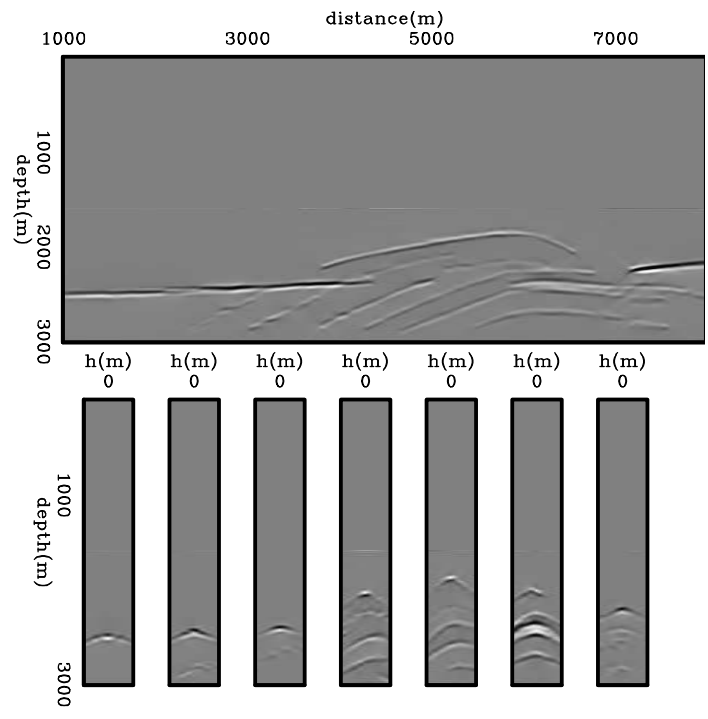


Figure 9: Selected reflectors used to model 35 pairs of ISPEW. **Guerra and Biondi** –

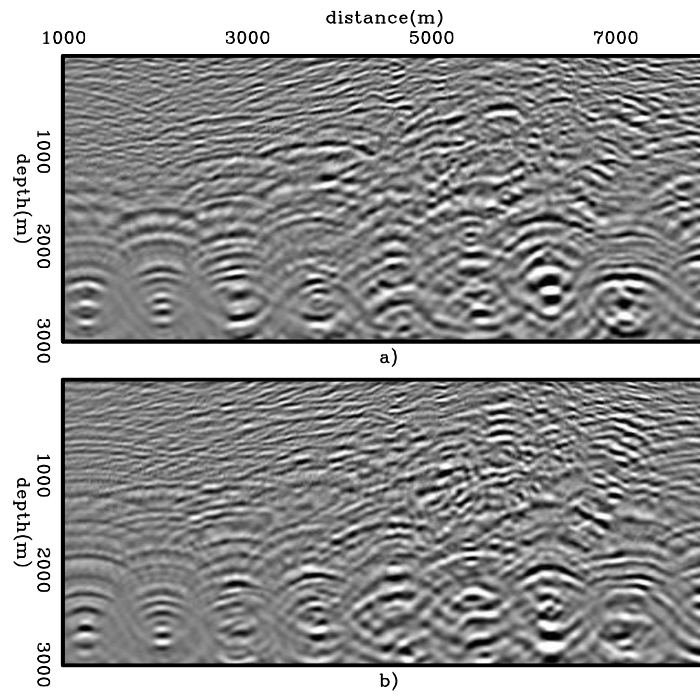


Figure 10: Snapshots of image-space generalized background wavefields: a) downward, and b) upward wavefields.

Guerra and Biondi –

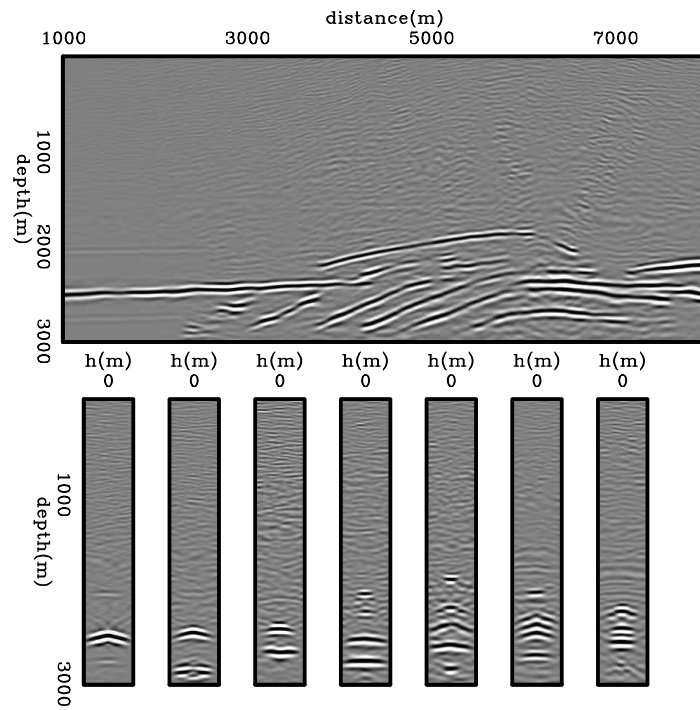


Figure 11: Background image computed with the image-space generalized background wavefields of Figure 10.

Guerra and Biondi –

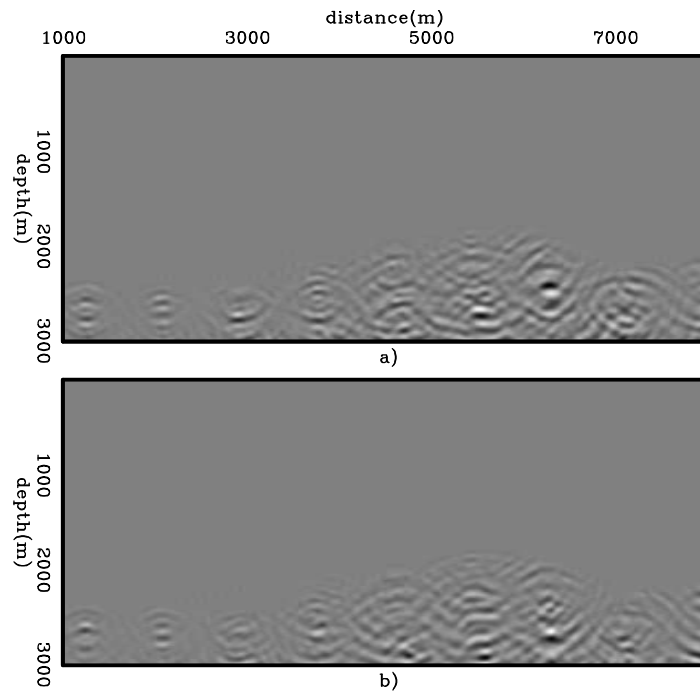


Figure 12: Snapshots of image-space generalized perturbed wavefields: a) source, and b) receiver.

Guerra and Biondi –

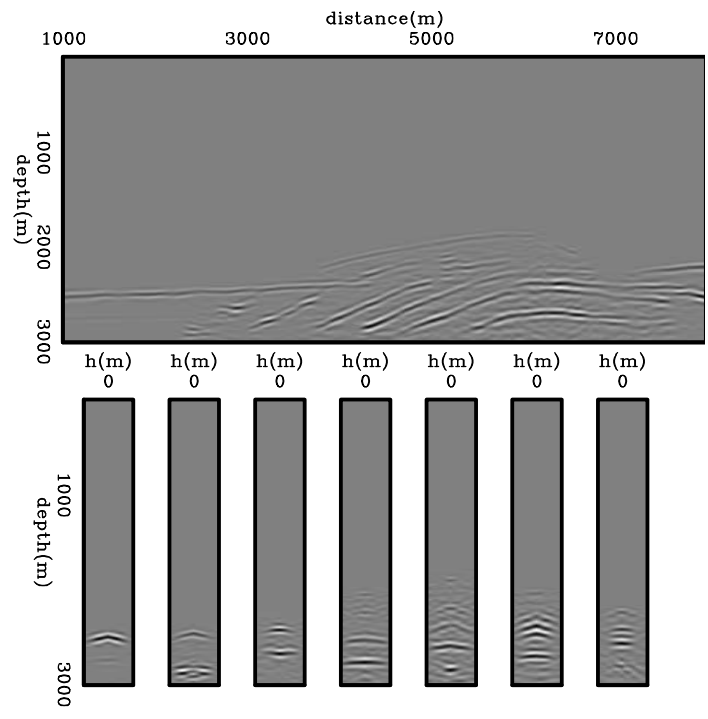


Figure 13: Perturbed image computed with equation 17. **Guerra and Biondi** –

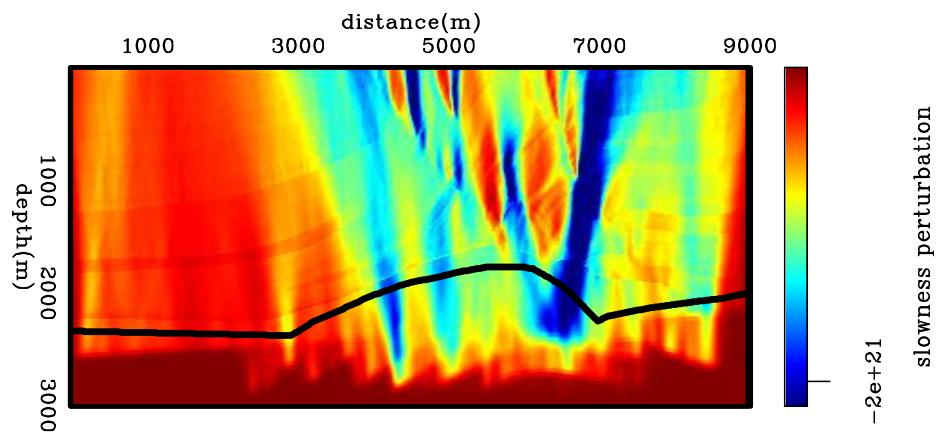


Figure 14: Slowness perturbation from back-projected image perturbations computed with 35 ISPEWs.

Guerra and Biondi –

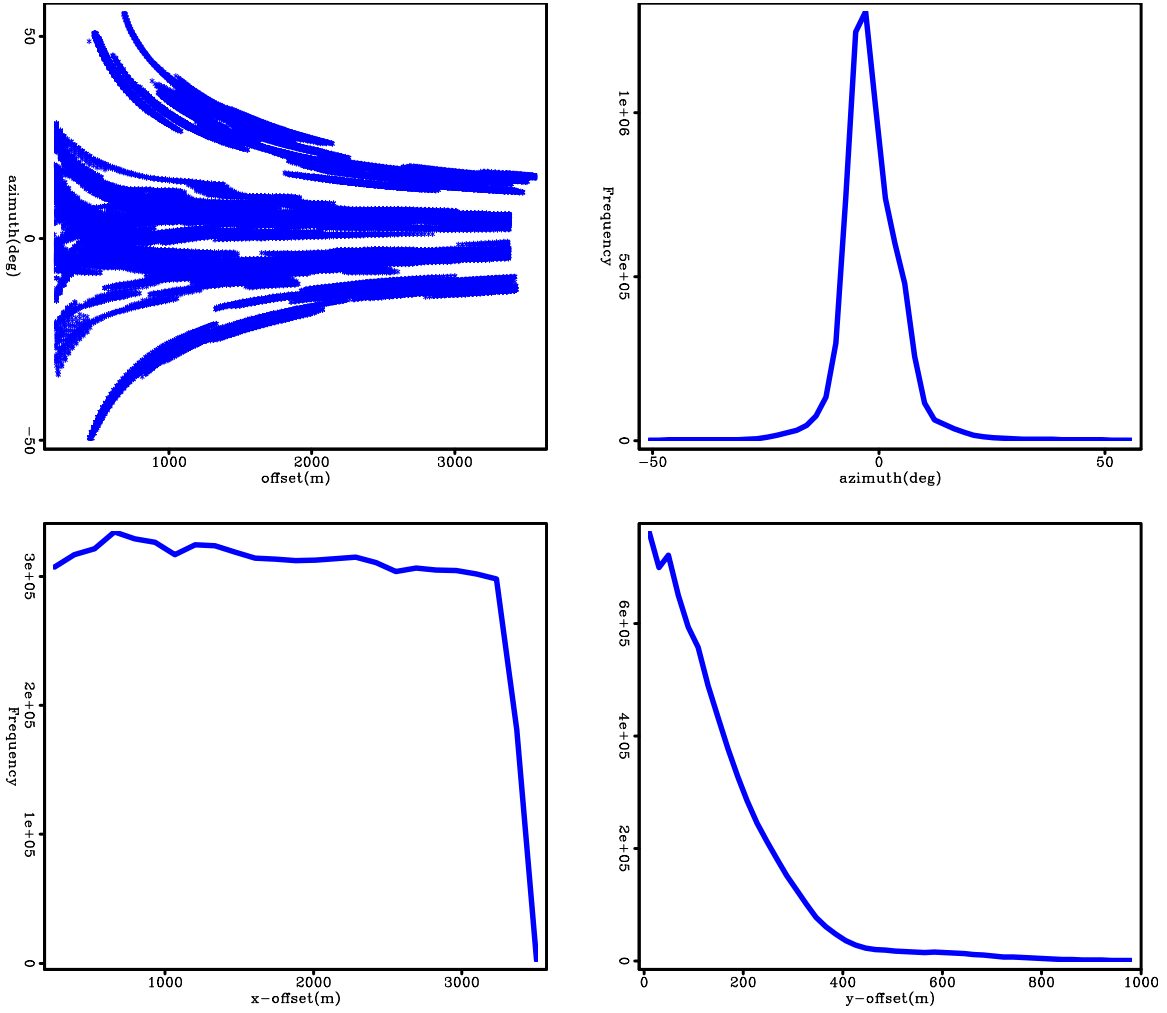


Figure 15: a) Offset – azimuth cross-plot, b) azimuth histogram, c) in-line offset histogram, and d) cross-line offset histogram.

Guerra and Biondi –

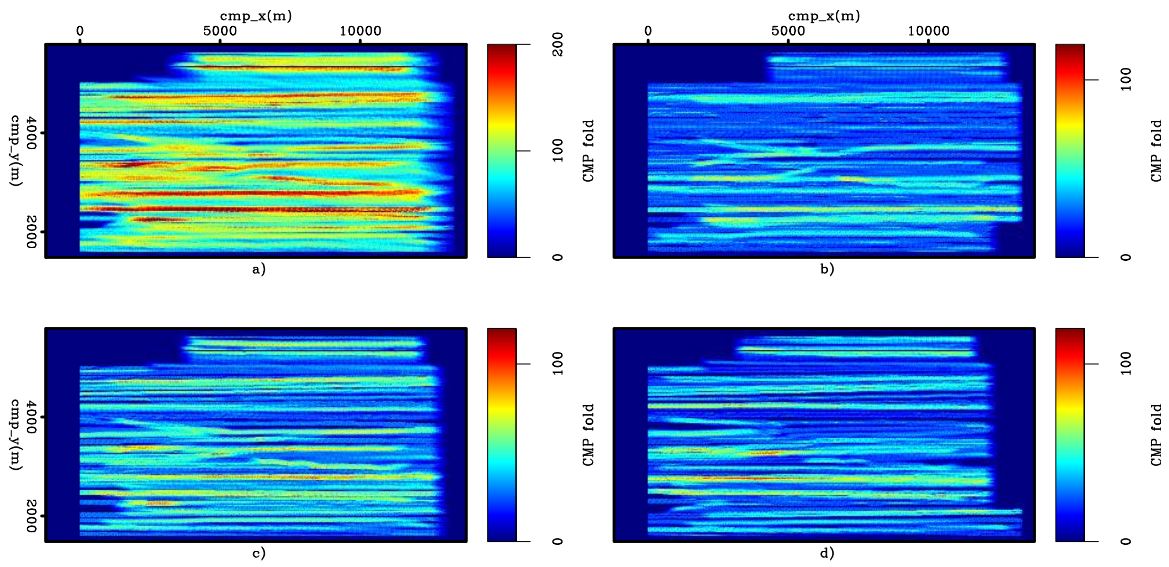


Figure 16: Fold of coverage plots: a) full offset, b) 0 – 1200 m offset, c) 1200 – 2400 m offset, and d) 2400 – 3600 m offset.

Guerra and Biondi –

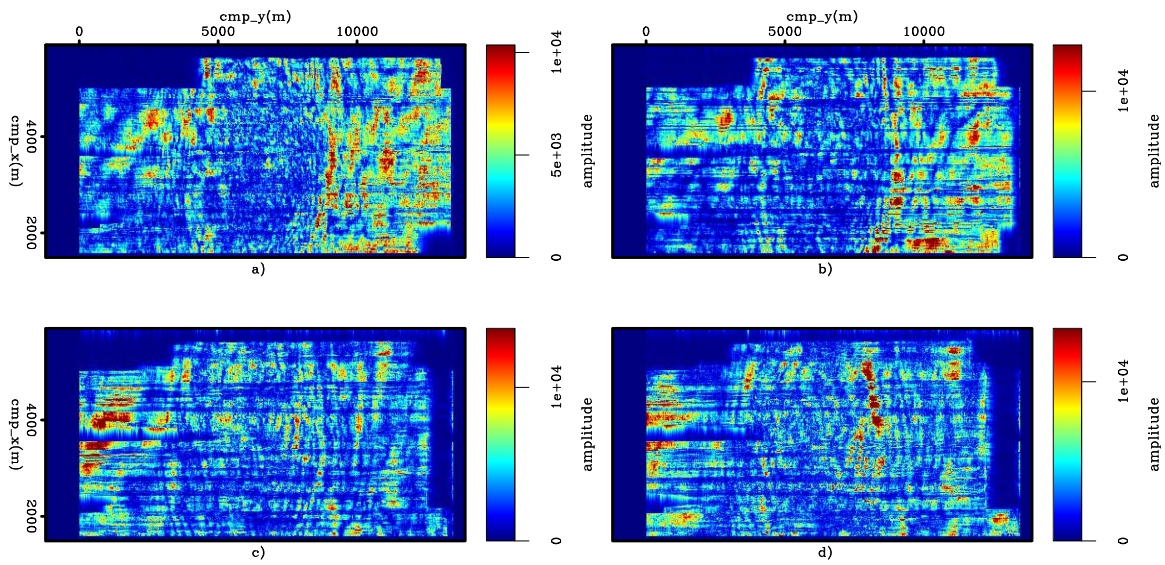


Figure 17: Time slices through the trace envelope for different offset cubes from the regularized data: a) offset 200m, b) offset 1200 m, c) offset 2400 m, and d) offset 3000 m.

Guerra and Biondi –

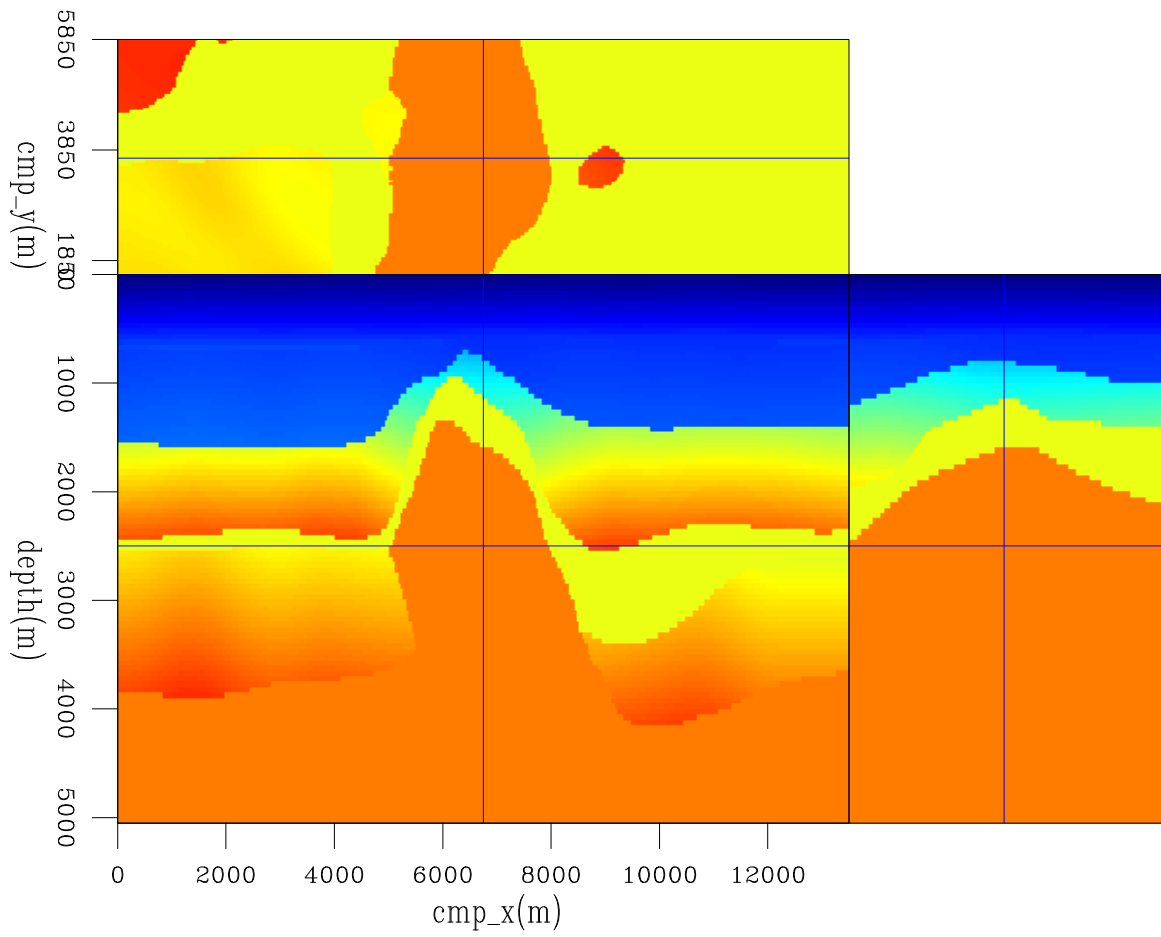


Figure 18: Slices through the IFP velocity model. **Guerra and Biondi** –

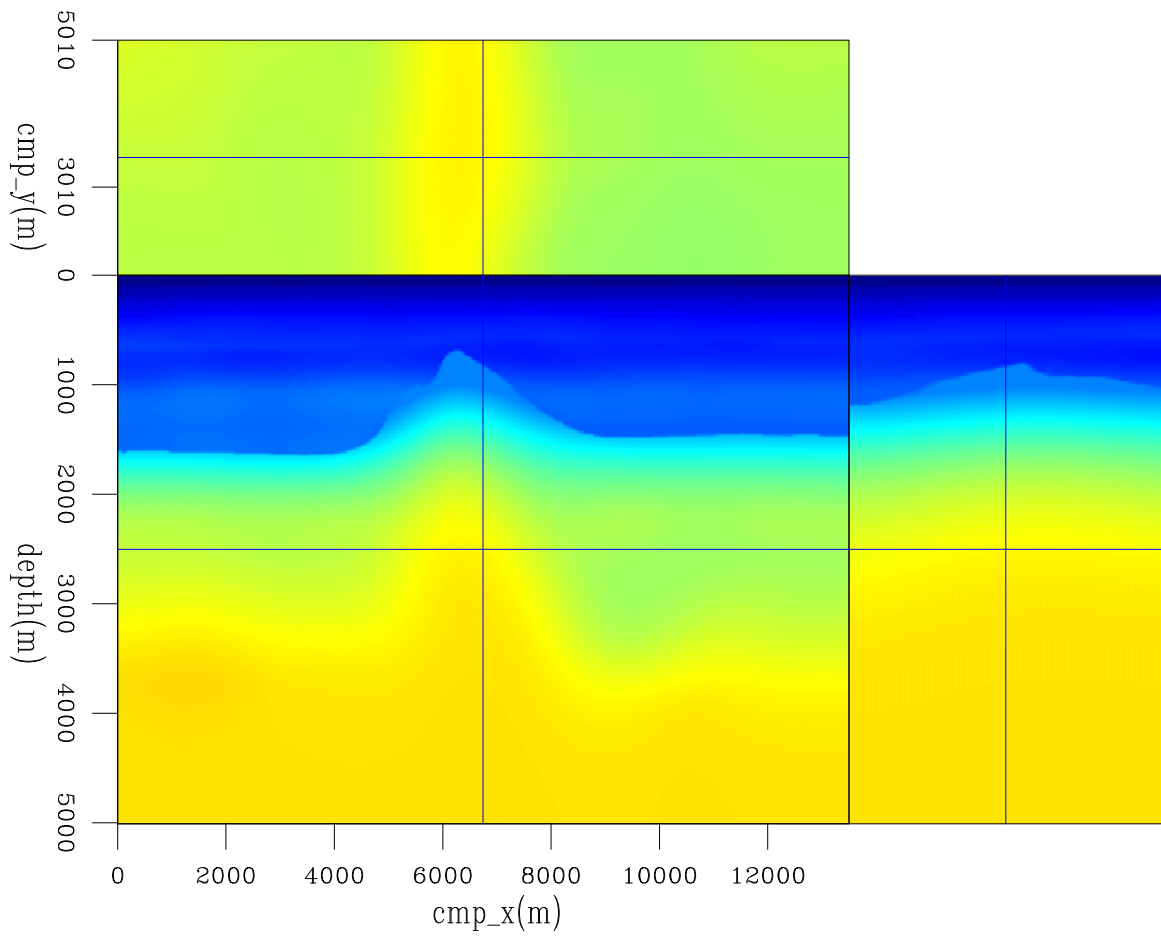


Figure 19: Slices through the initial velocity model used in 3D-ISWET.

Guerra and Biondi –

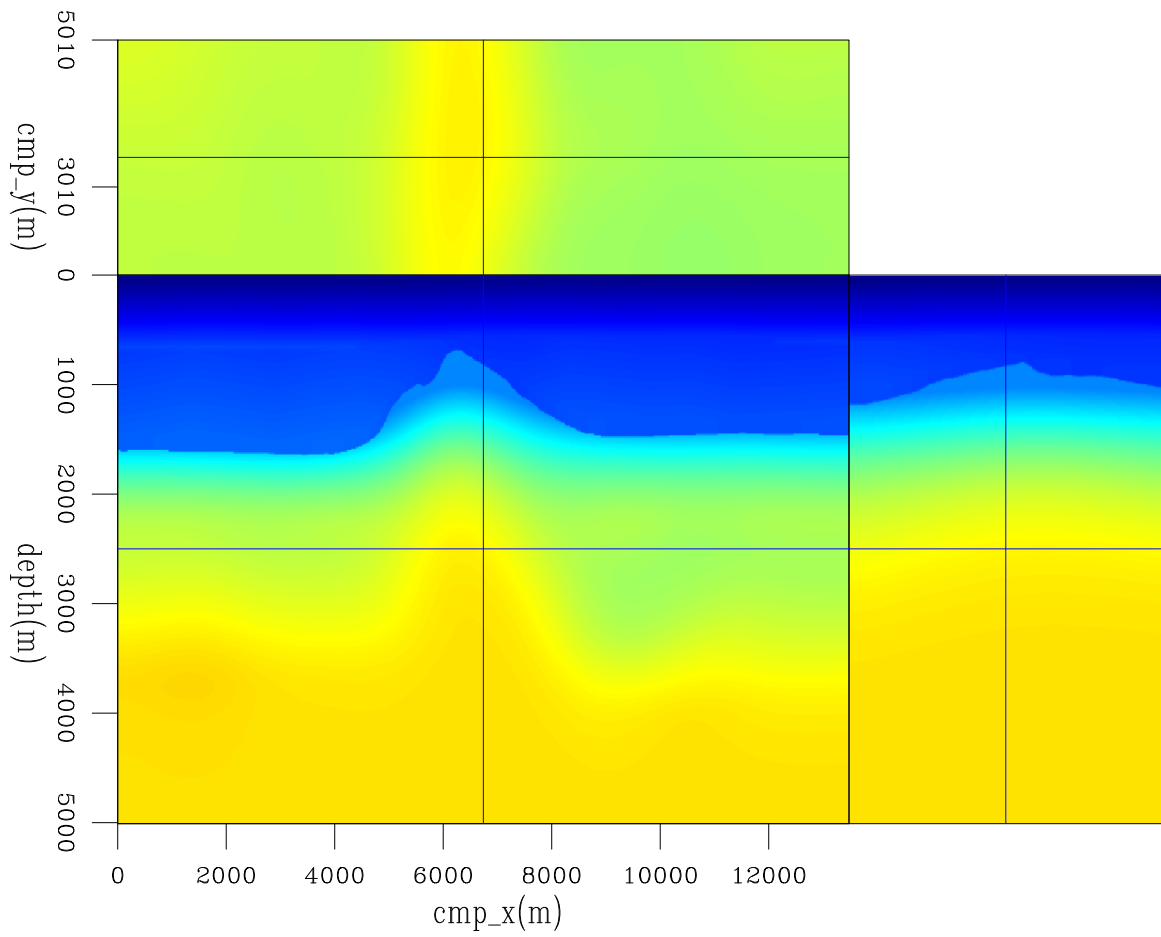


Figure 20: Slices through an initial velocity model generated with the same procedures as that for Figure 19, except for the velocity above the chalk, which is the original velocity.

Guerra and Biondi –

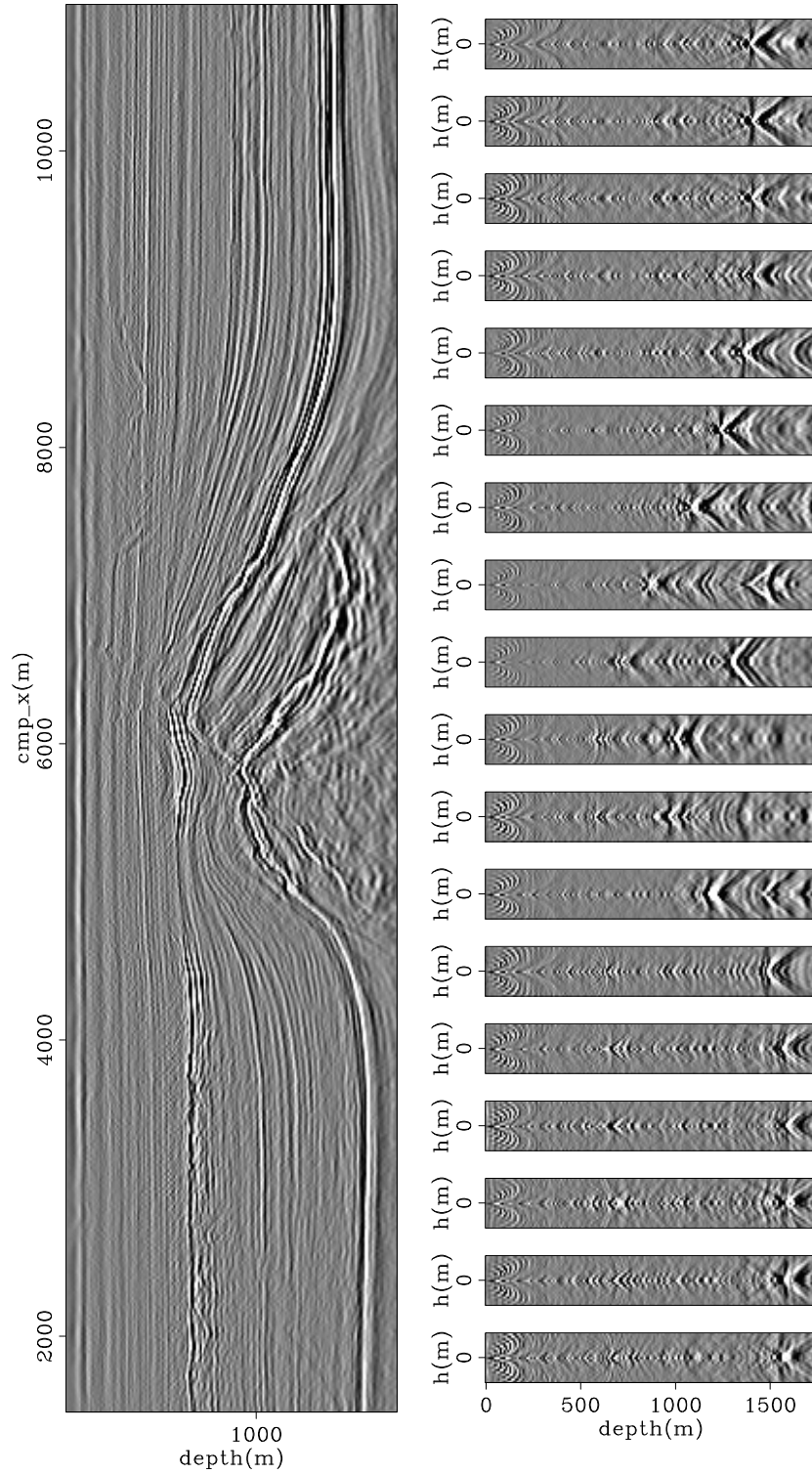


Figure 21: Image computed with the velocity model of Figure 20. The top panel is the zero-subsurface offset section and the panel at the bottom are the SODCIGs.

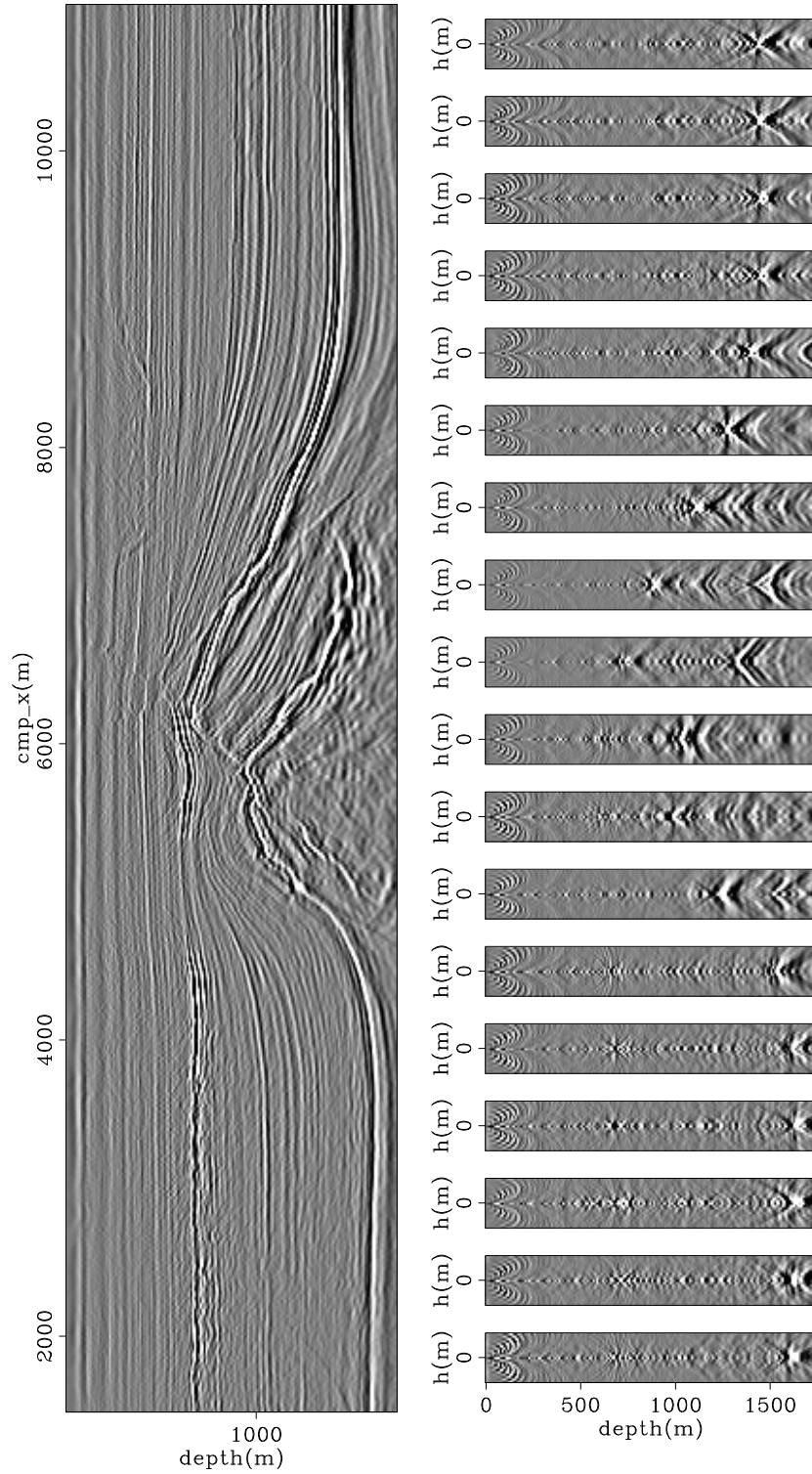


Figure 22: Image computed with the velocity model of Figure 19. The left panel is the zero-subsurface offset section and the panels on the right are the SODCIGs. Compare with Figure 21.

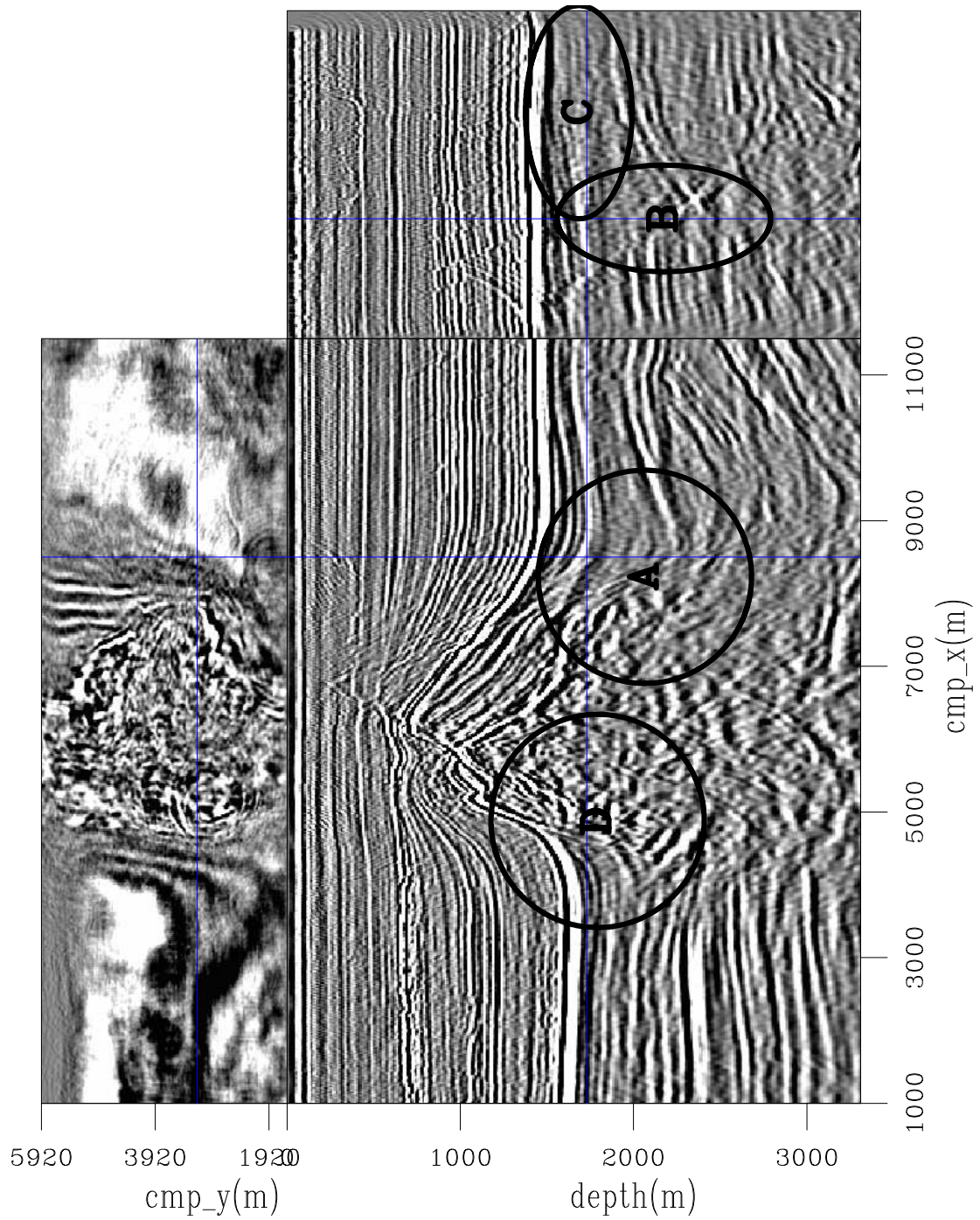


Figure 23: Slices through the CAM image with the initial velocity model of Figure 19. Notice poorly collapsed diffractions close to the salt flank (A and D), and poorly imaged faults (B and C) caused by migrating with an inaccurate velocity.

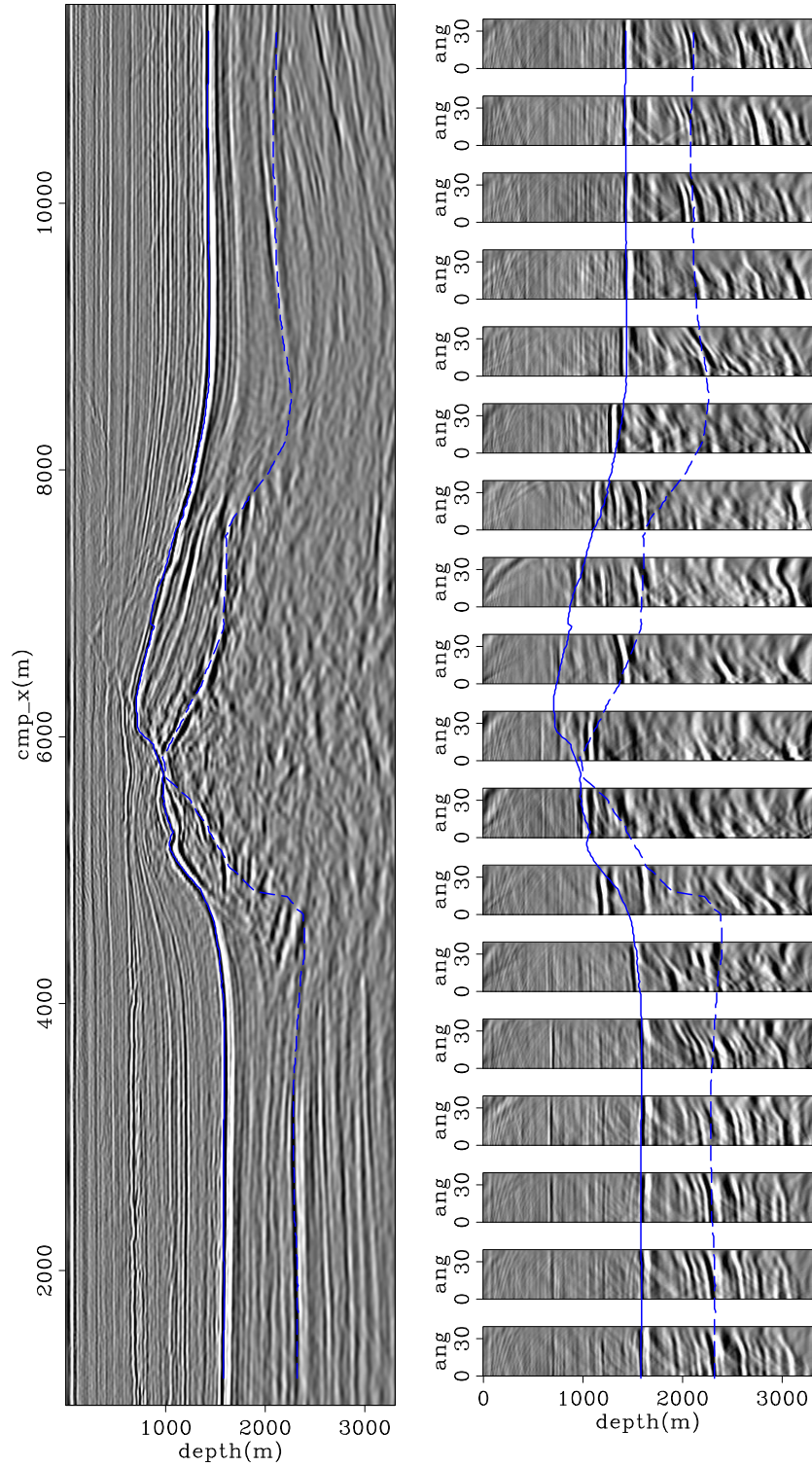


Figure 24: In-line 3180 of the CAM image with the initial velocity model of Figure 19. On the left is the zero-subsurface offset section, and on the right ADCIGs. Notice the strong residual moveout on the ADCIGs. The continuous blue line is the top of chalk, and the

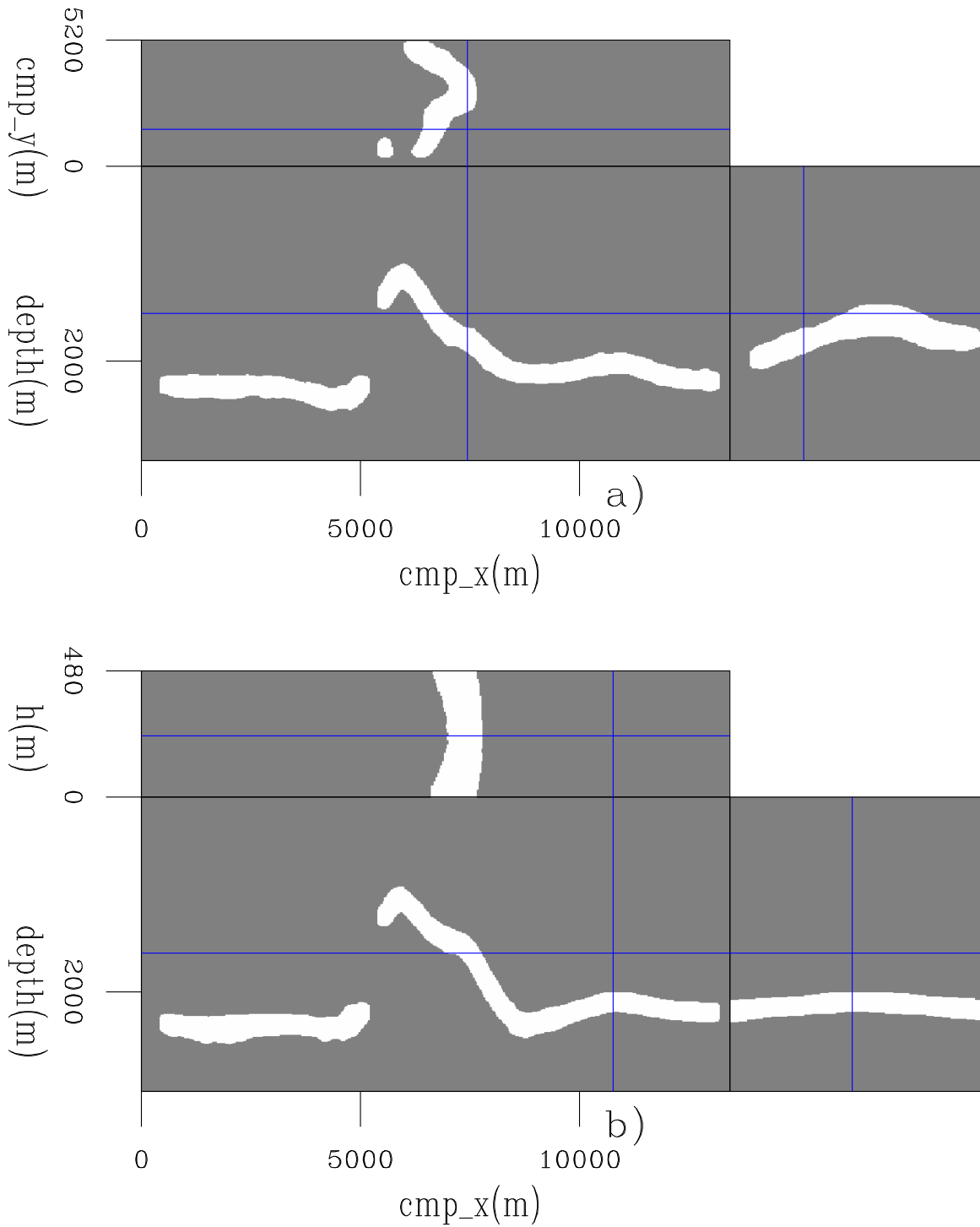


Figure 25: Slices through the prestack-mask operator to select the base of chalk, showing:
a) the zero subsurface offset, and b) the in-line 3520.

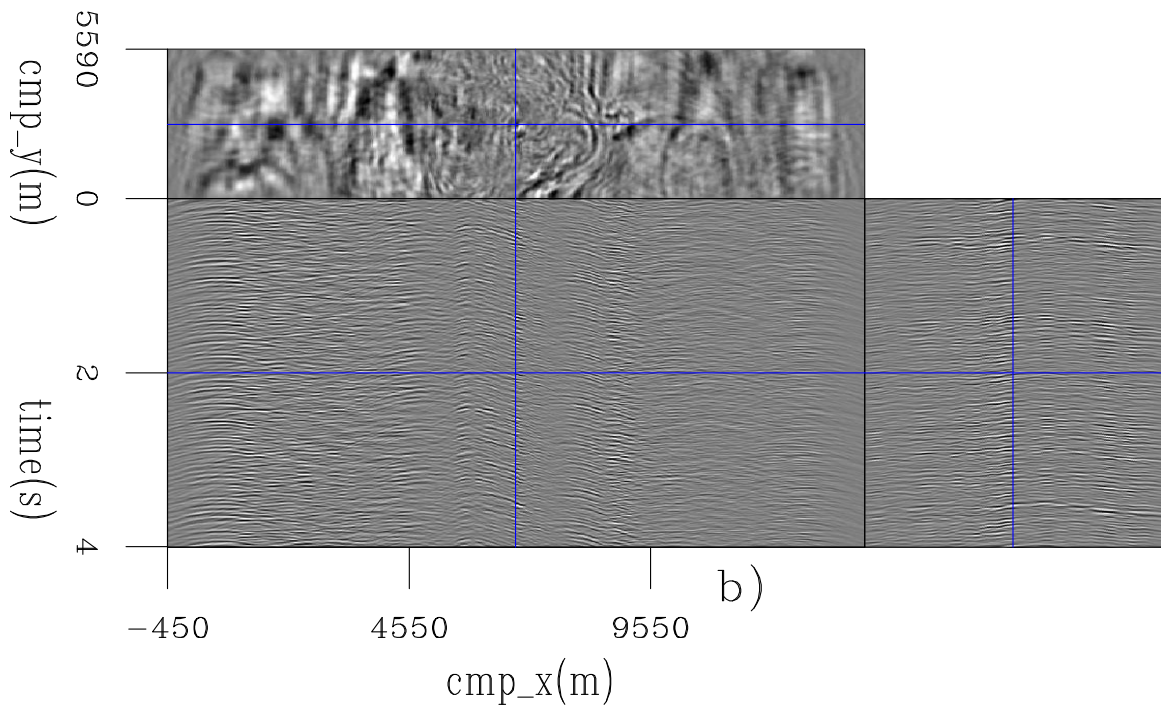
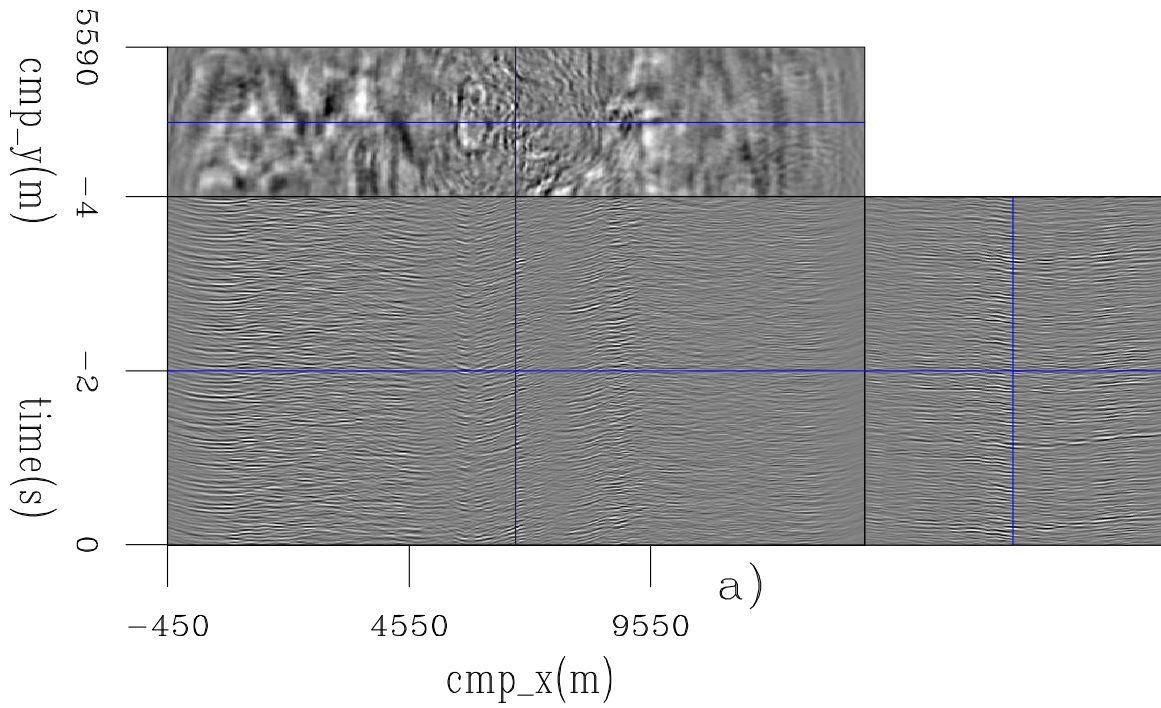


Figure 26: A pair of 3D source (a) and receiver (b) ISPEWs computed for the base of chalk.

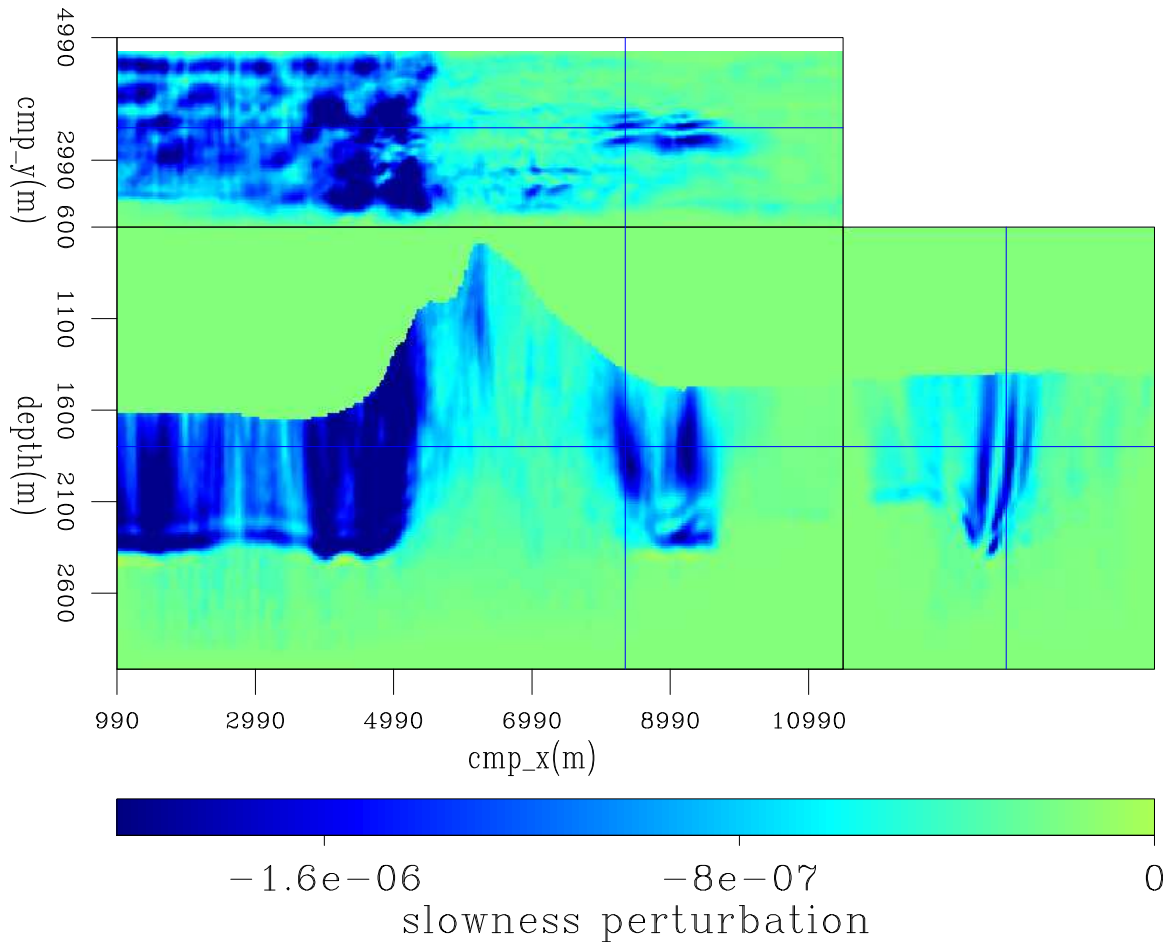


Figure 27: Slowness perturbation without smoothing and without extracting the signed square root from the initial conditions for the modeling of 30 pairs of ISPEWs.

Guerra and Biondi –

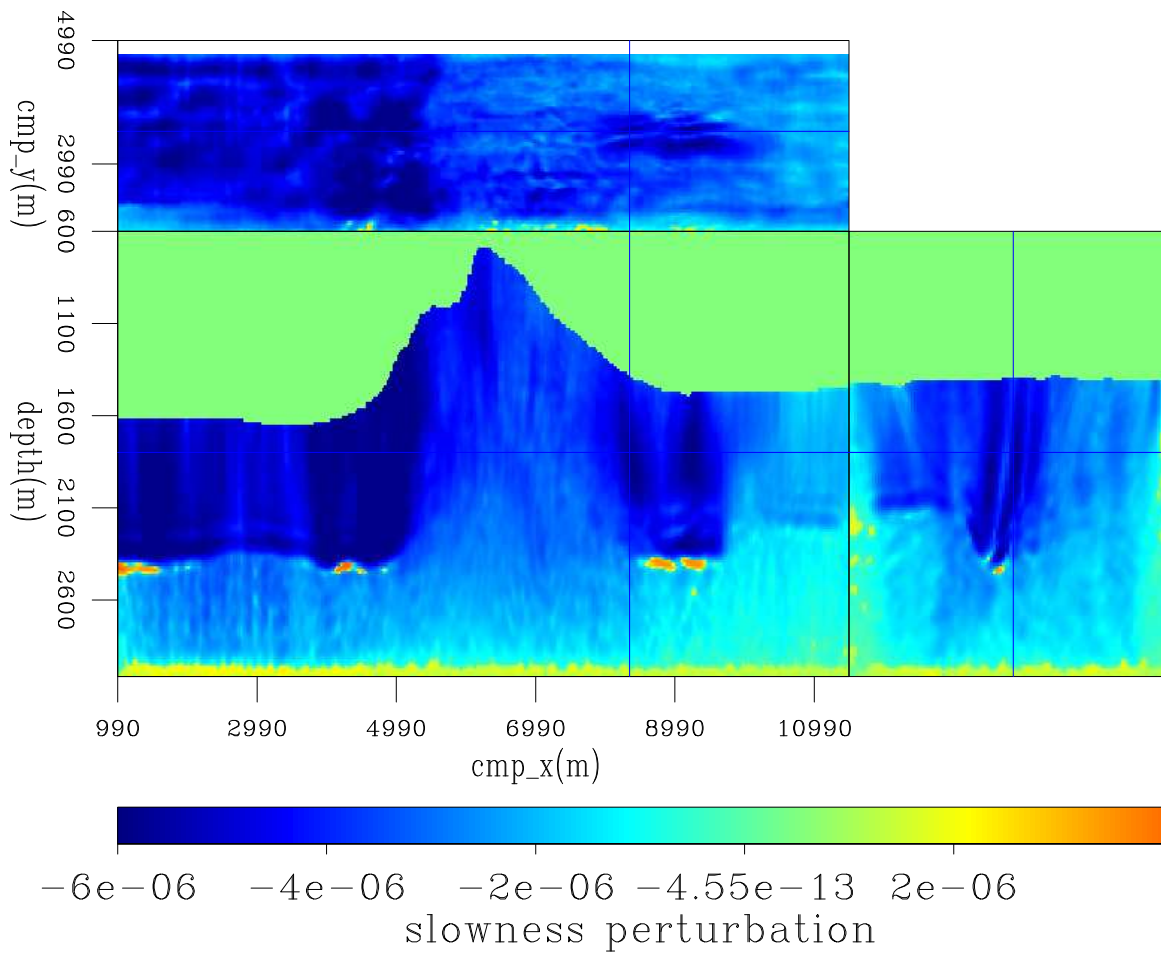


Figure 28: Slowness perturbation without smoothing and extracting the signed fourth root of the gradient.

Guerra and Biondi –

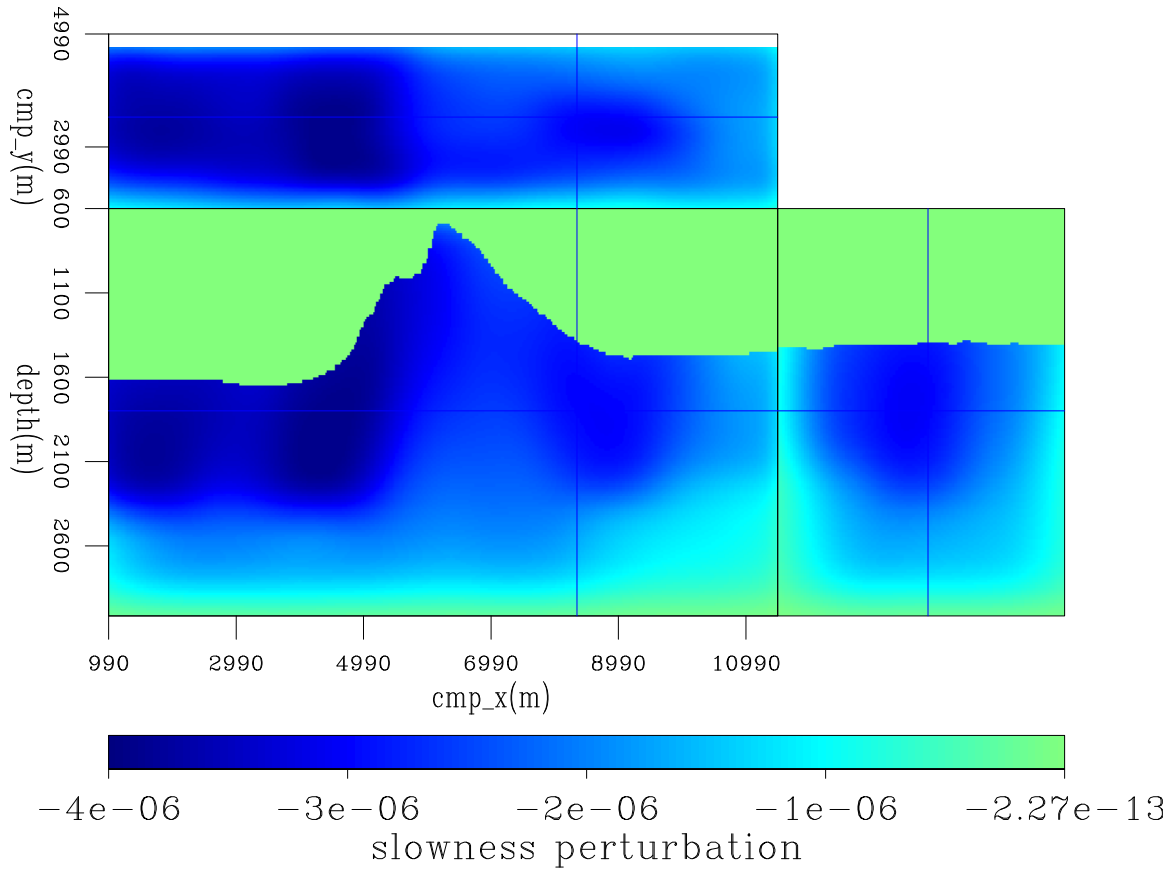


Figure 29: Slowness perturbation after B-spline smoothing the slowness perturbation of Figure 28.

Guerra and Biondi –

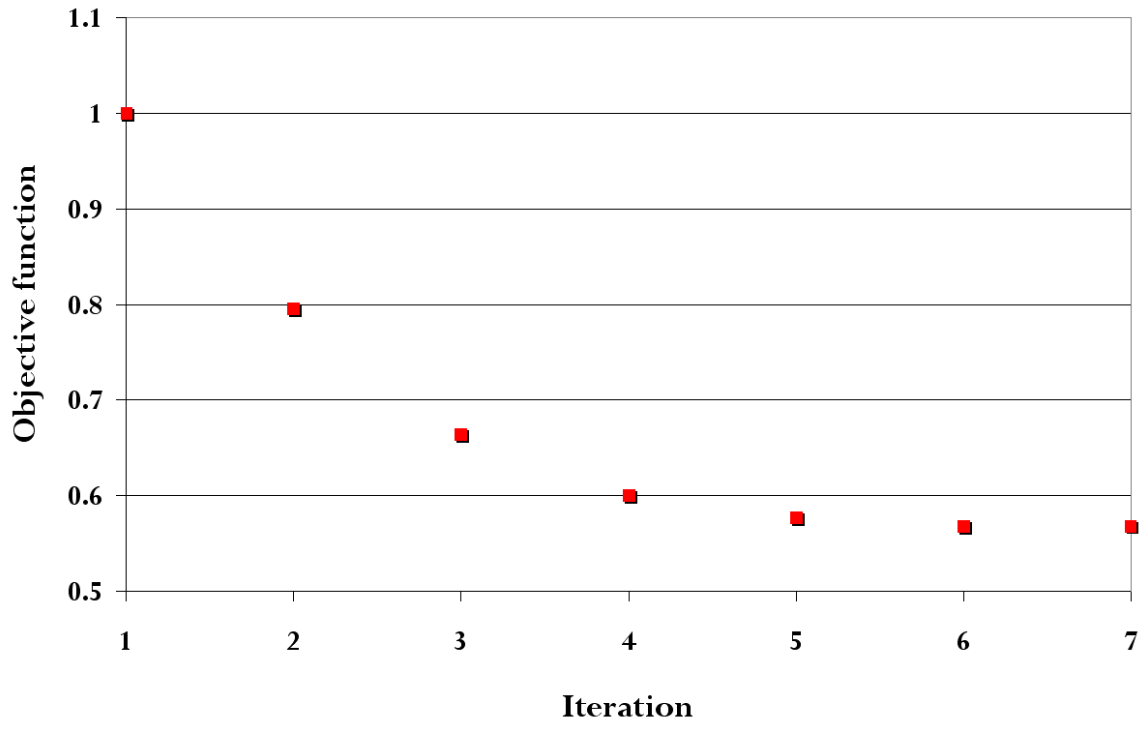


Figure 30: Evolution of the DVSA objective function for the first run of ISWET for the base of chalk.

Guerra and Biondi –

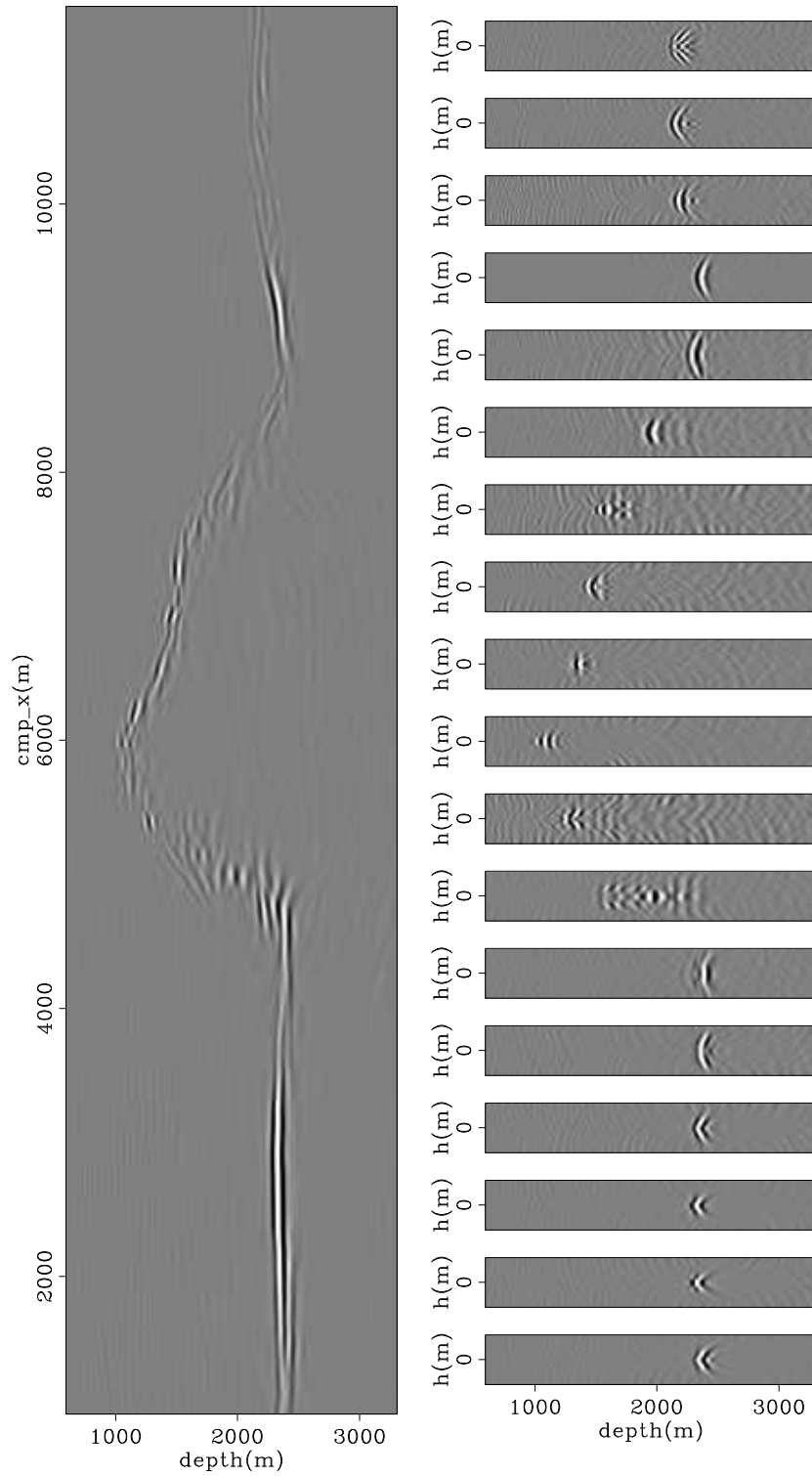


Figure 31: In-line 3520 of the initial background image of the first run of ISWET for the base of chalk.

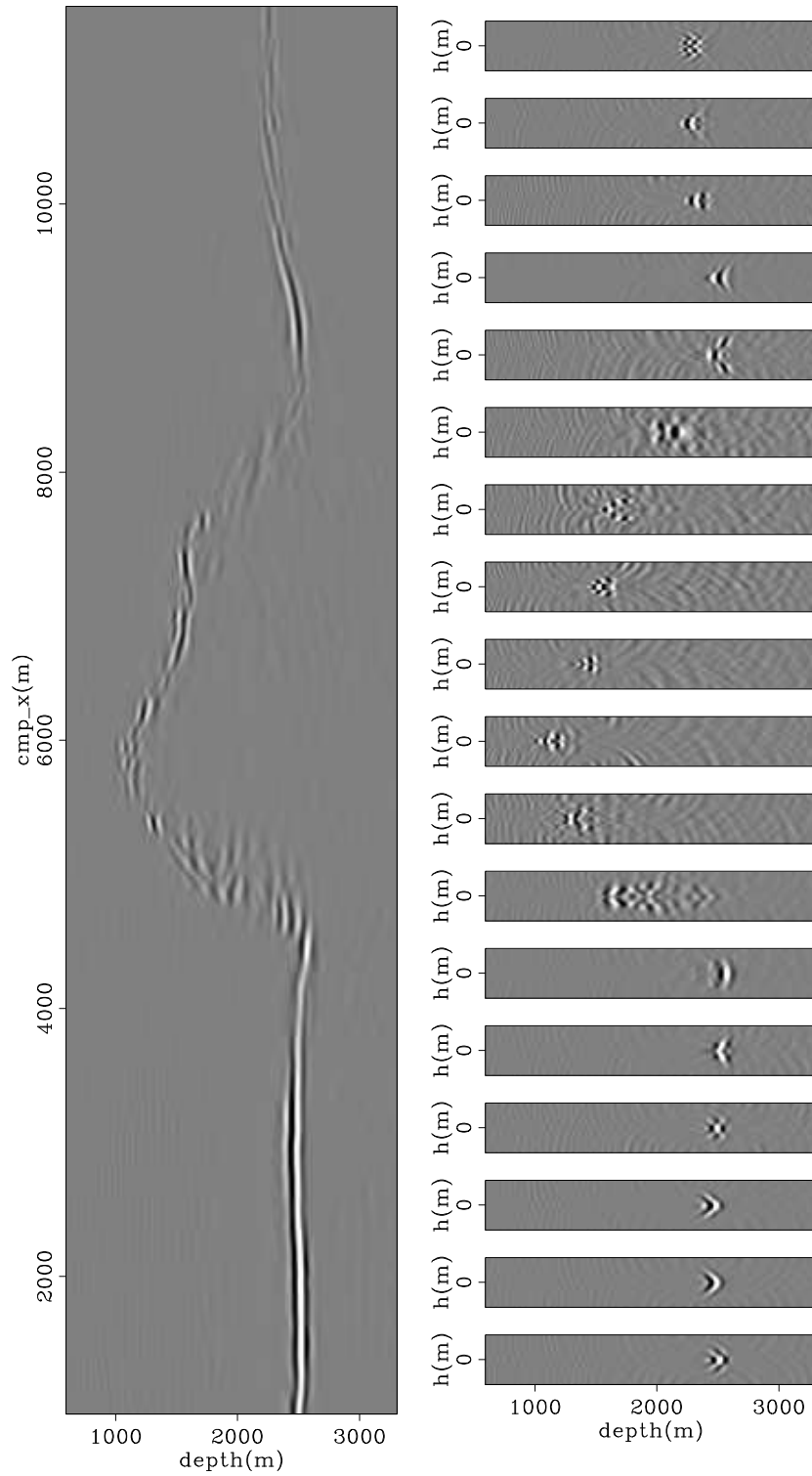


Figure 32: In-line 3520 of the background image computed with the optimized velocity model of the first run of ISWET for the base of chalk.

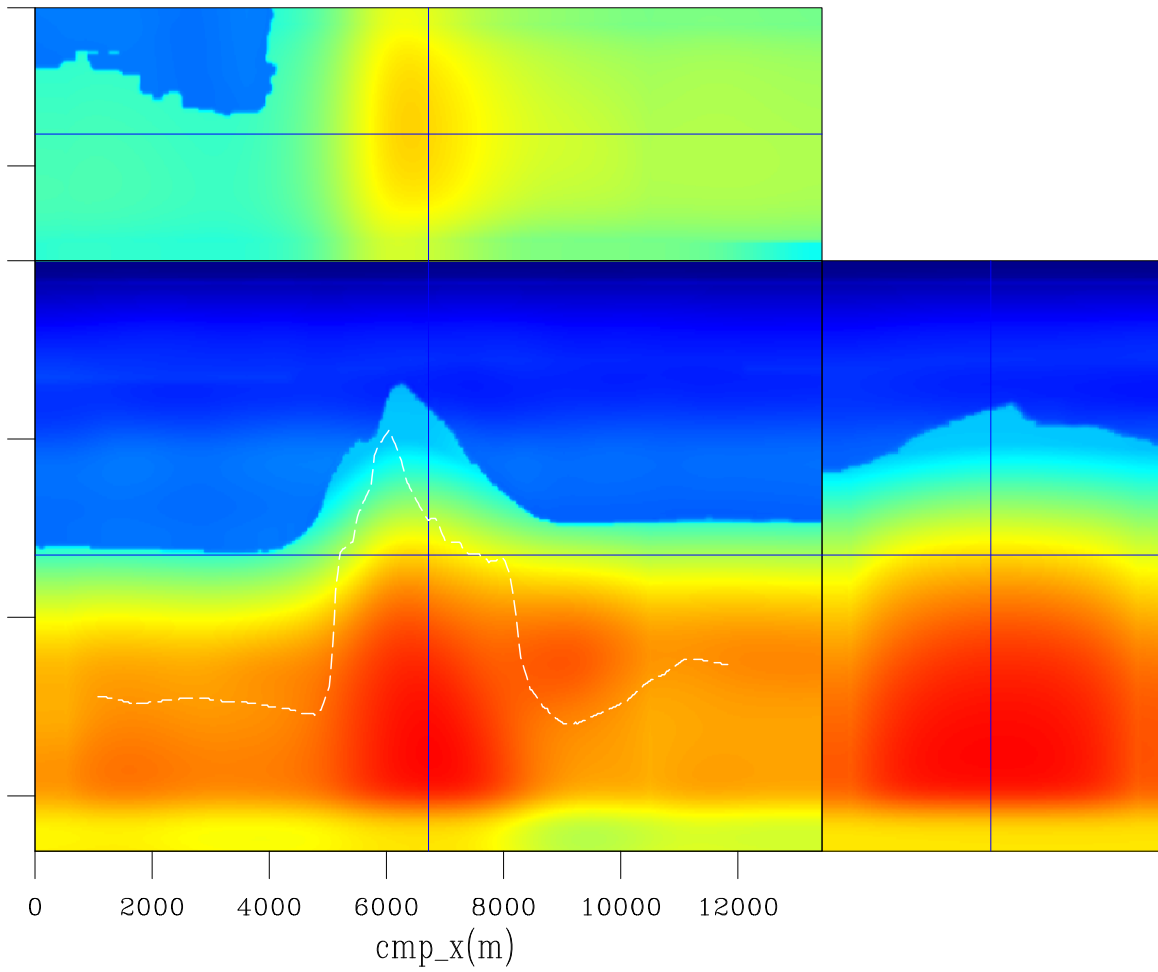


Figure 33: Slices through the optimized velocity from the first run of ISWET for the base of chalk. The dashed white line approximately represents the base of chalk.

Guerra and Biondi –

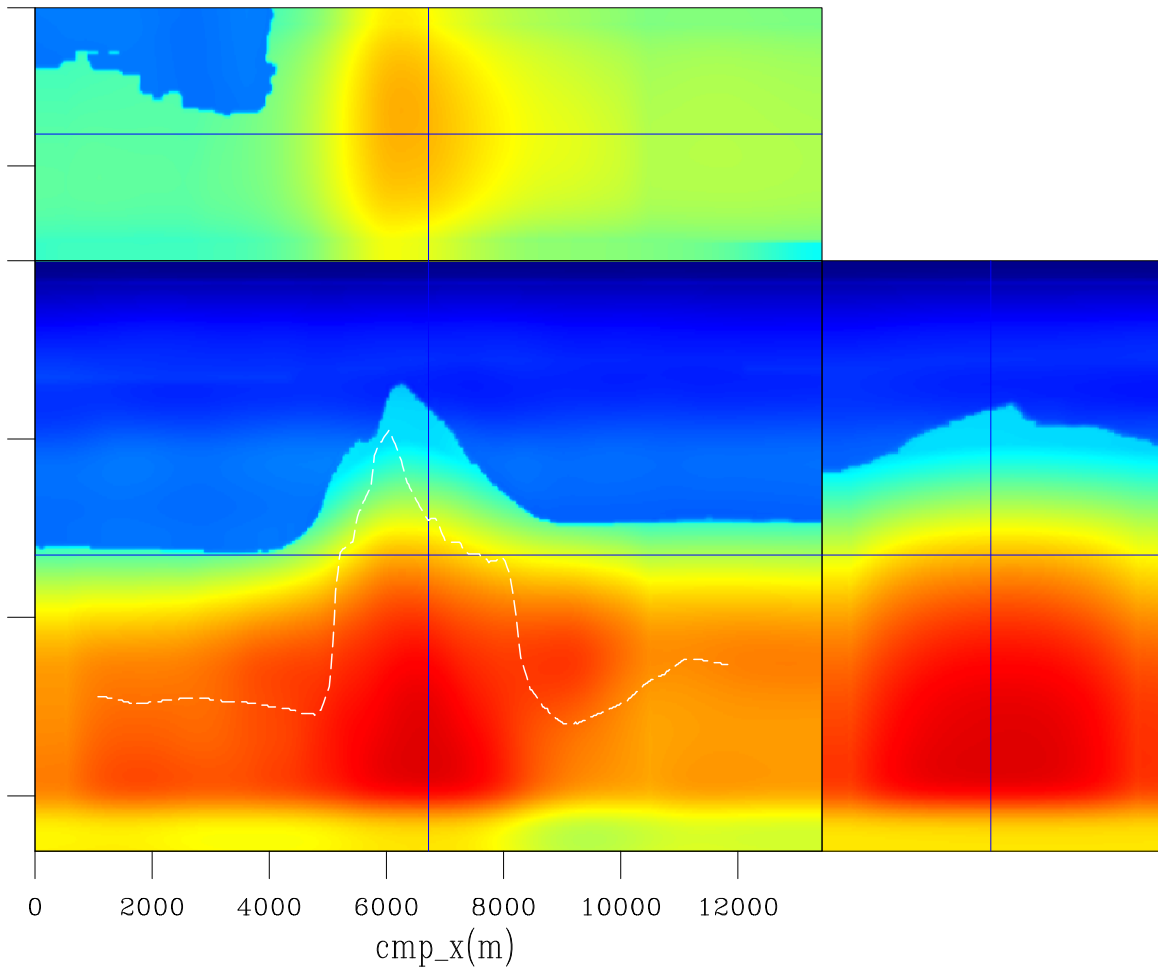


Figure 34: Slices through the optimized velocity from the second run of ISWET for the base of chalk. The dashed white line approximately represents the base of chalk.

Guerra and Biondi –

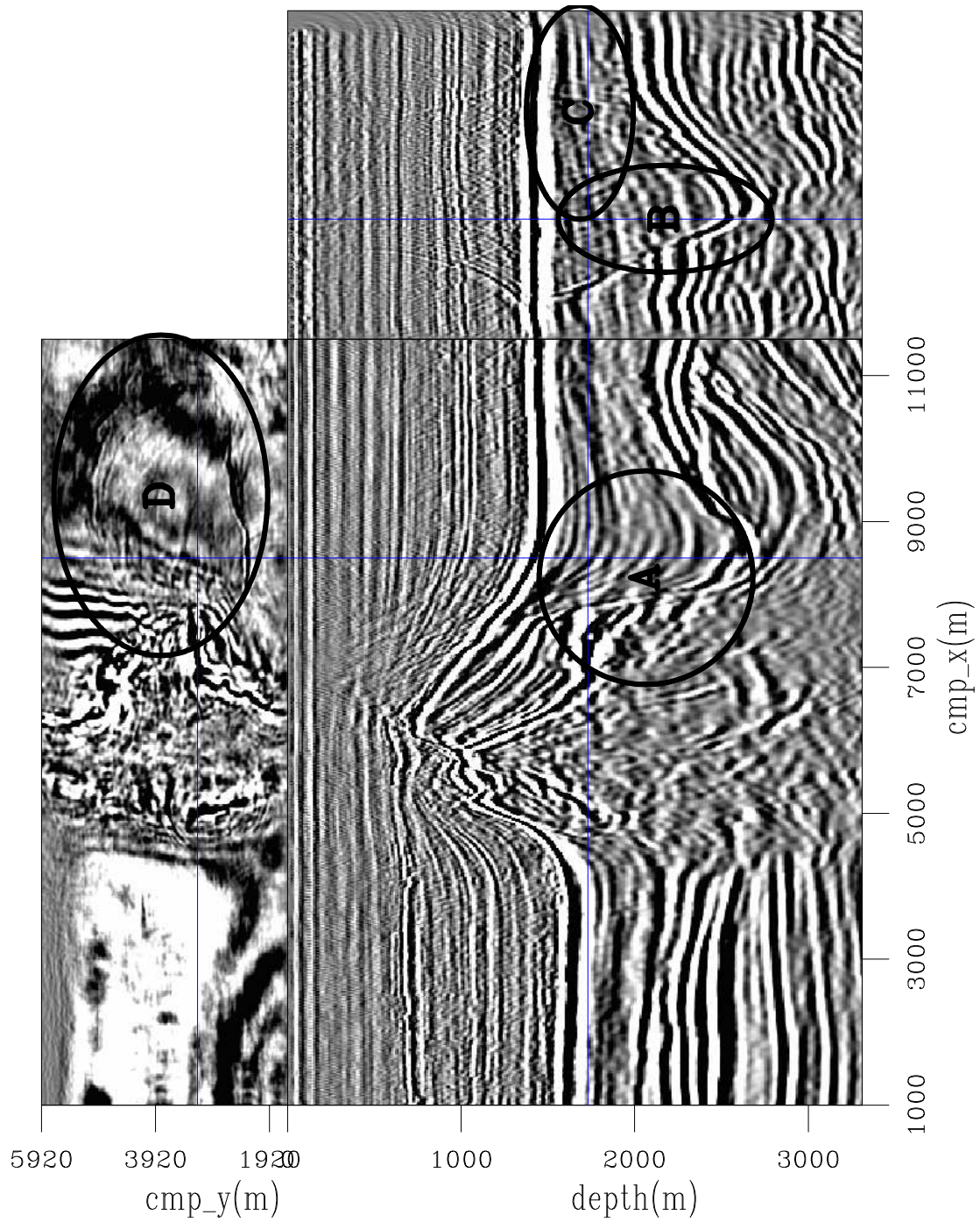


Figure 35: Slices through the CAM image with the optimized velocity model of Figure 34. Notice the imaging of a big fault close to the salt flank (A), and the focusing of a complex fault system (B, C, and D).

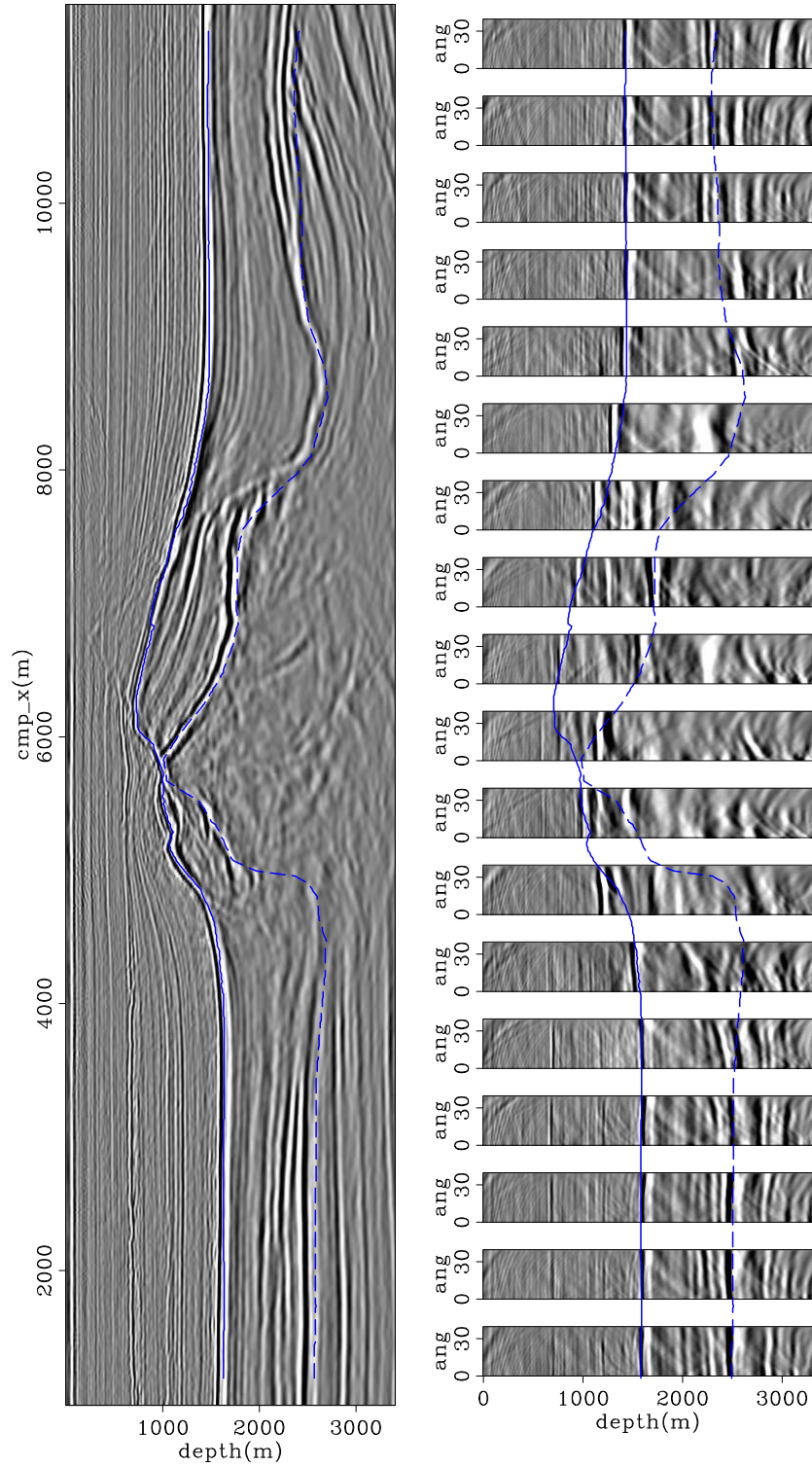


Figure 36: In-line 3180 of the CAM image with the optimized velocity model of Figure 34.

On the left is the zero-subsurface offset section, and on the right ADCIGs. Notice flatter

reflectors in the ADCIGs compared to those in Figure 24. The continuous blue line is the

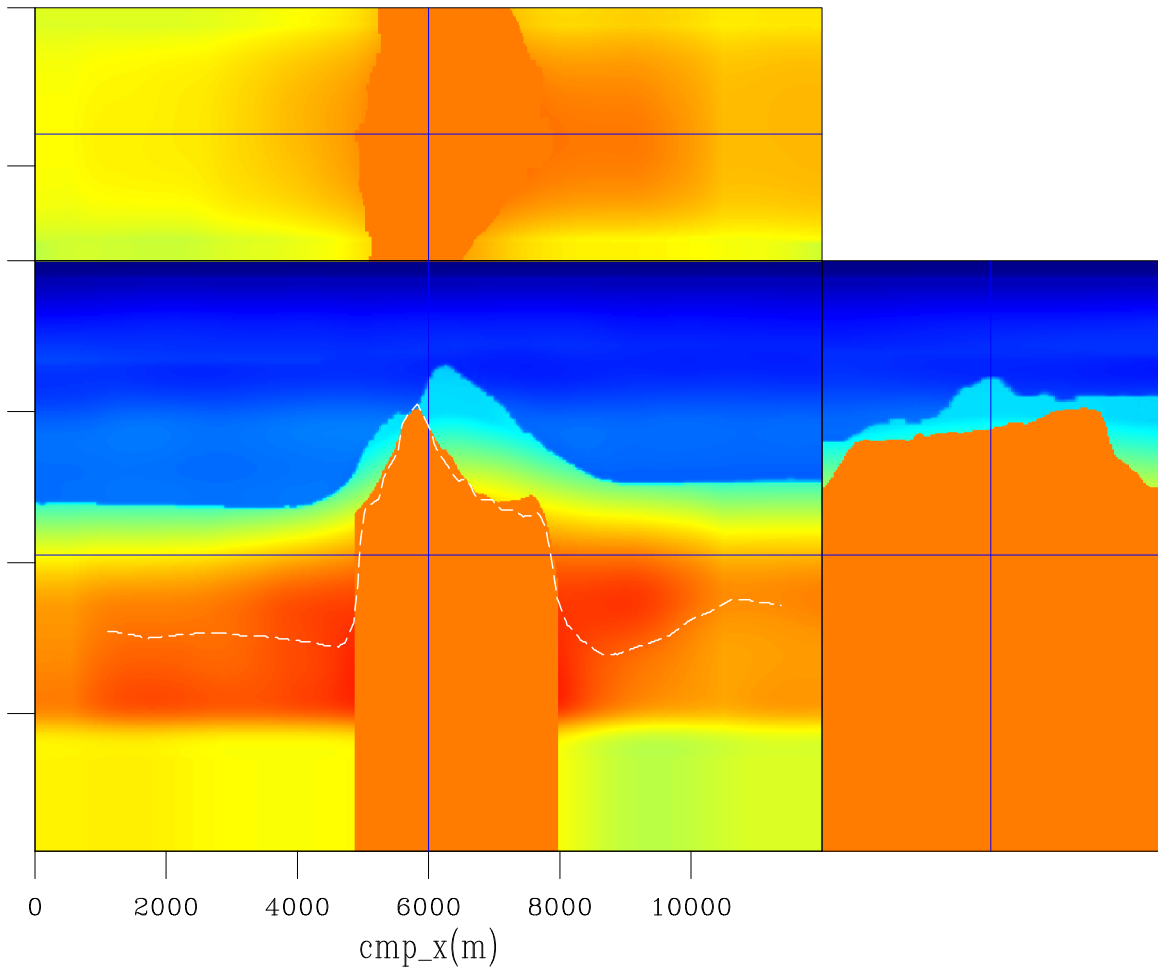


Figure 37: Slices through the velocity volume after salt flooding. The dashed white line approximately represents the base of chalk.

Guerra and Biondi –

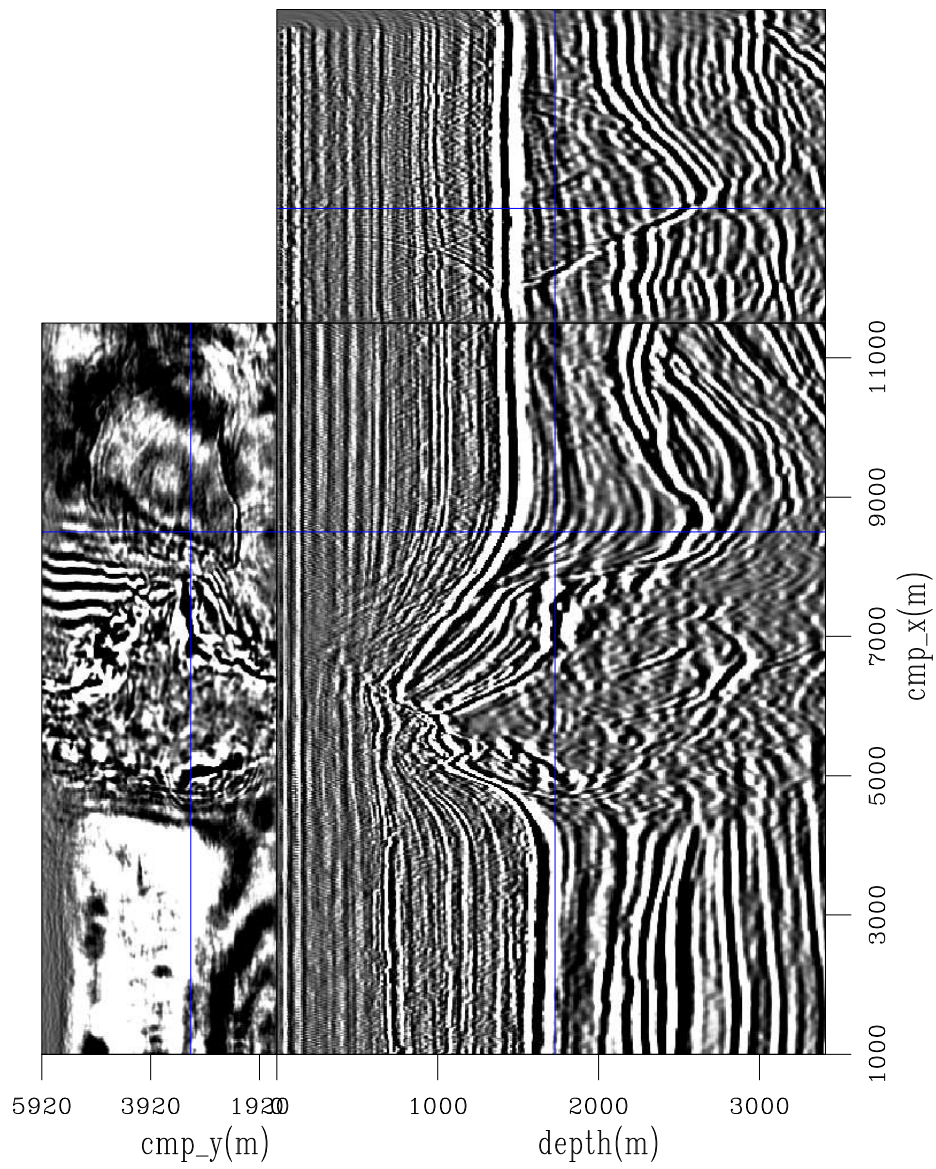


Figure 38: Slices through the CAM migrated image computed with the salt flooding velocity model of Figure 37.

Guerra and Biondi –

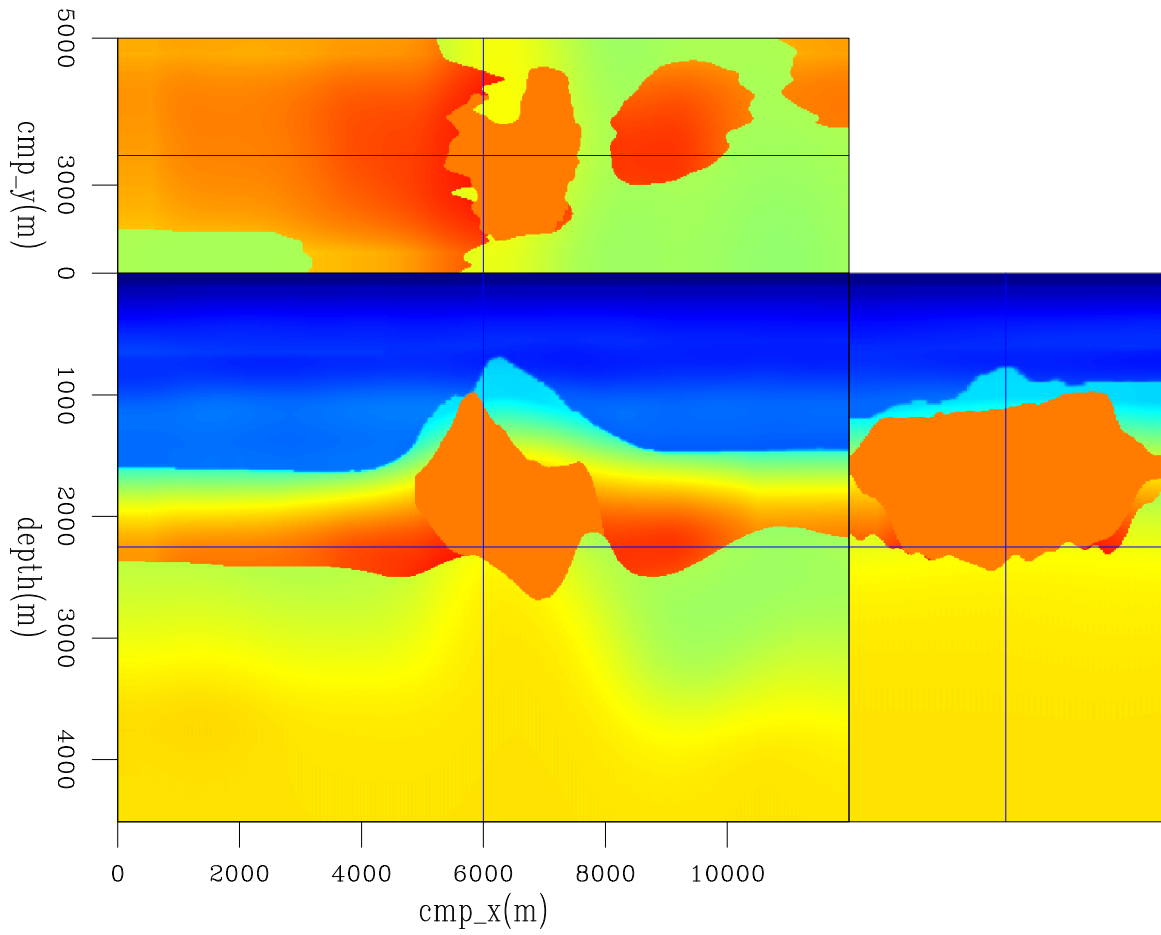


Figure 39: Slices through the velocity volume after interpretation of the base of salt.

Guerra and Biondi –

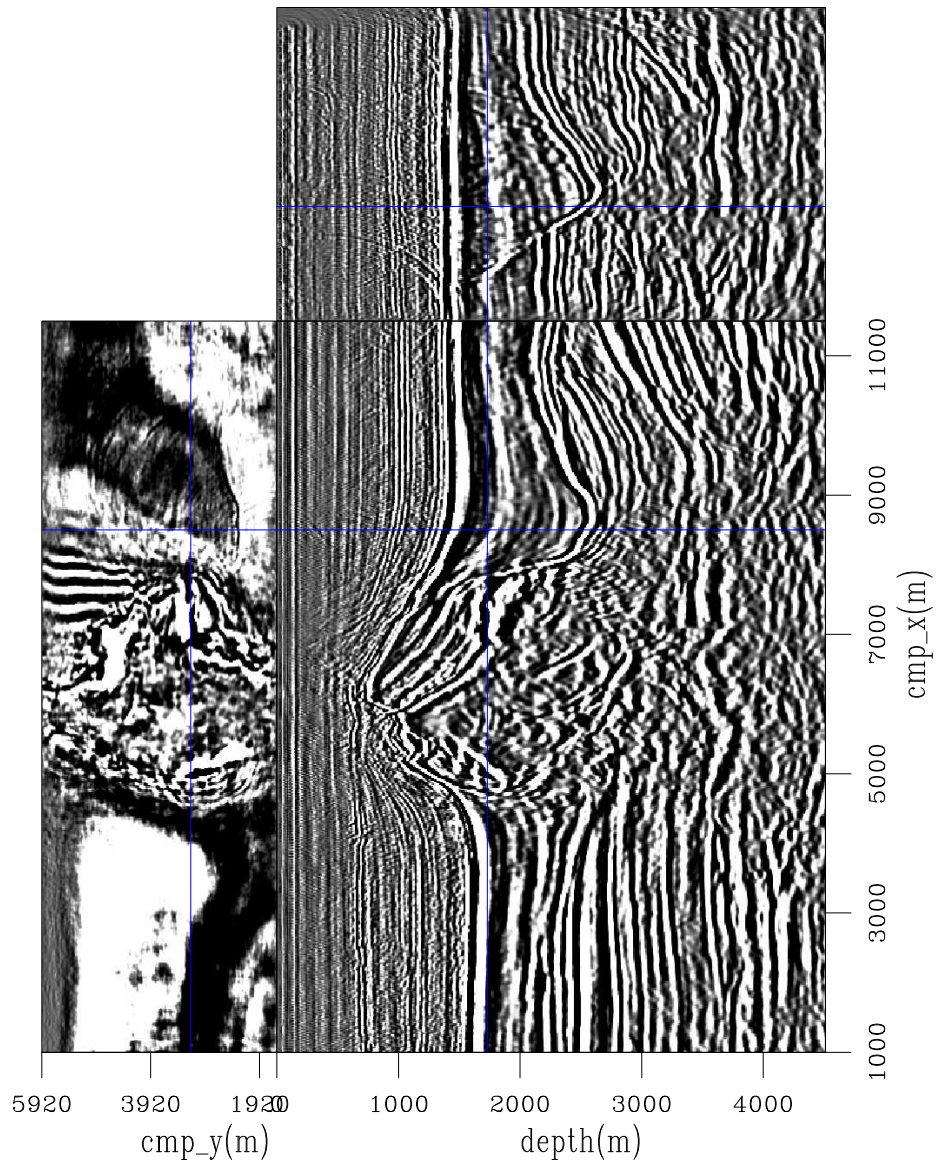


Figure 40: Slices through the CAM migrated image computed with the velocity model of Figure 39.

Guerra and Biondi –

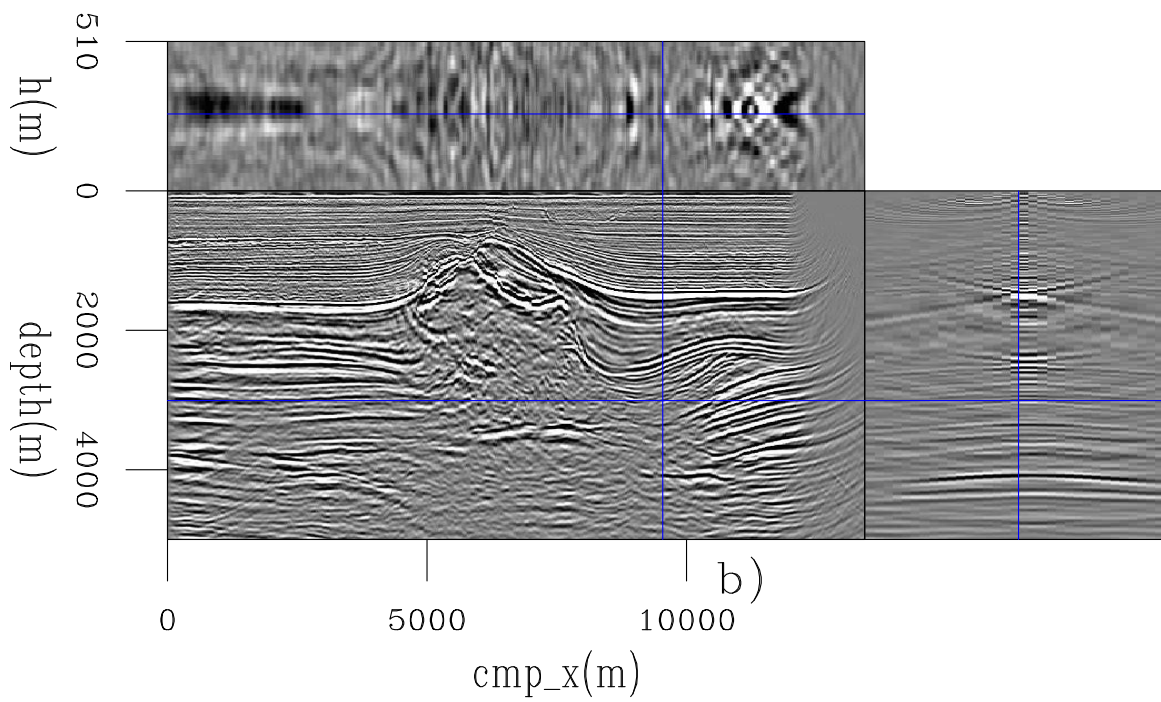
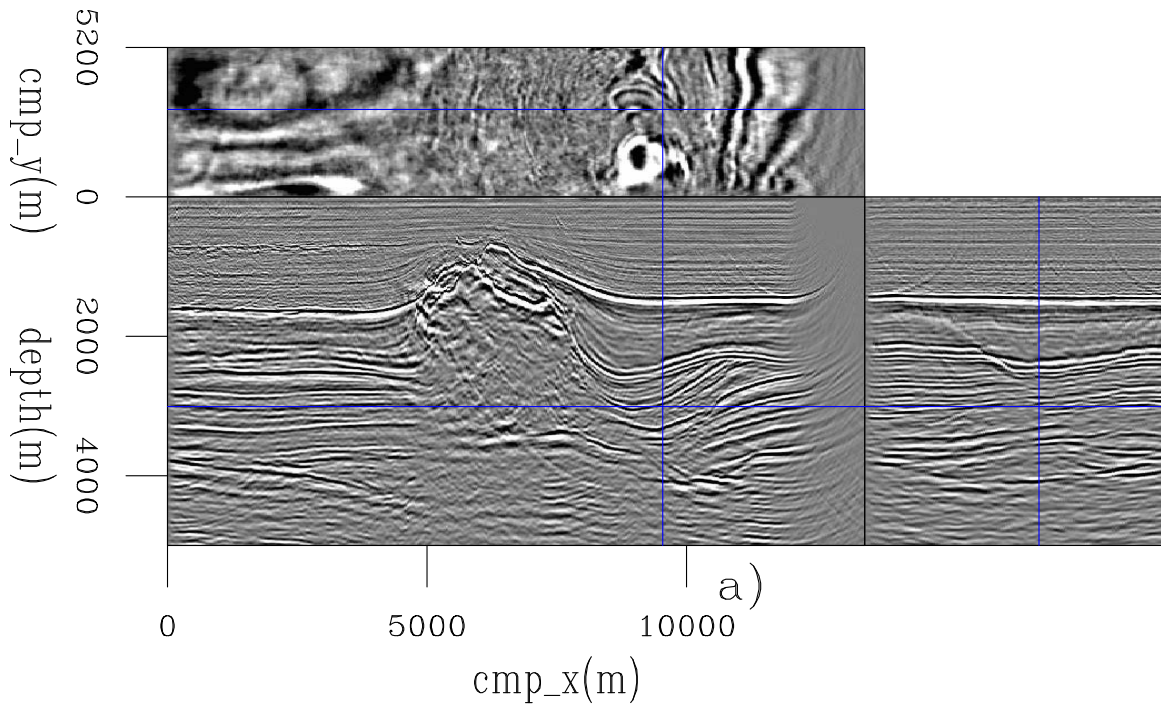


Figure 41: Slices through the prestack image computed with the migration velocity of Figure 39: a) the zero subsurface offset, and b) the in-line 3520.

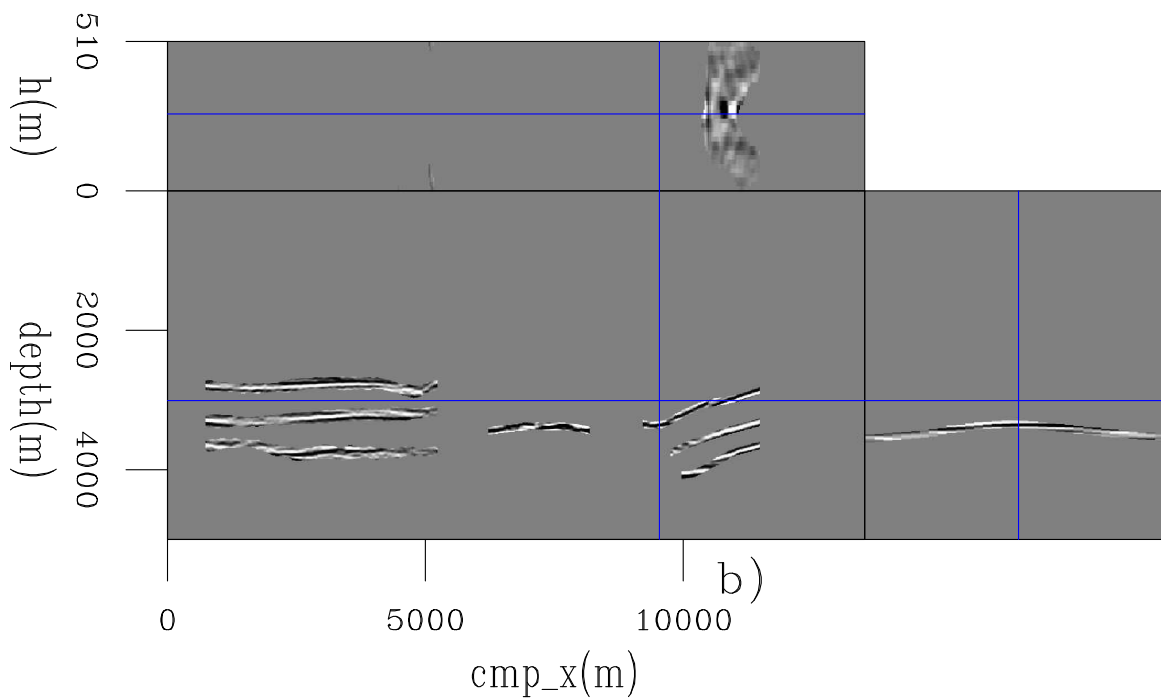
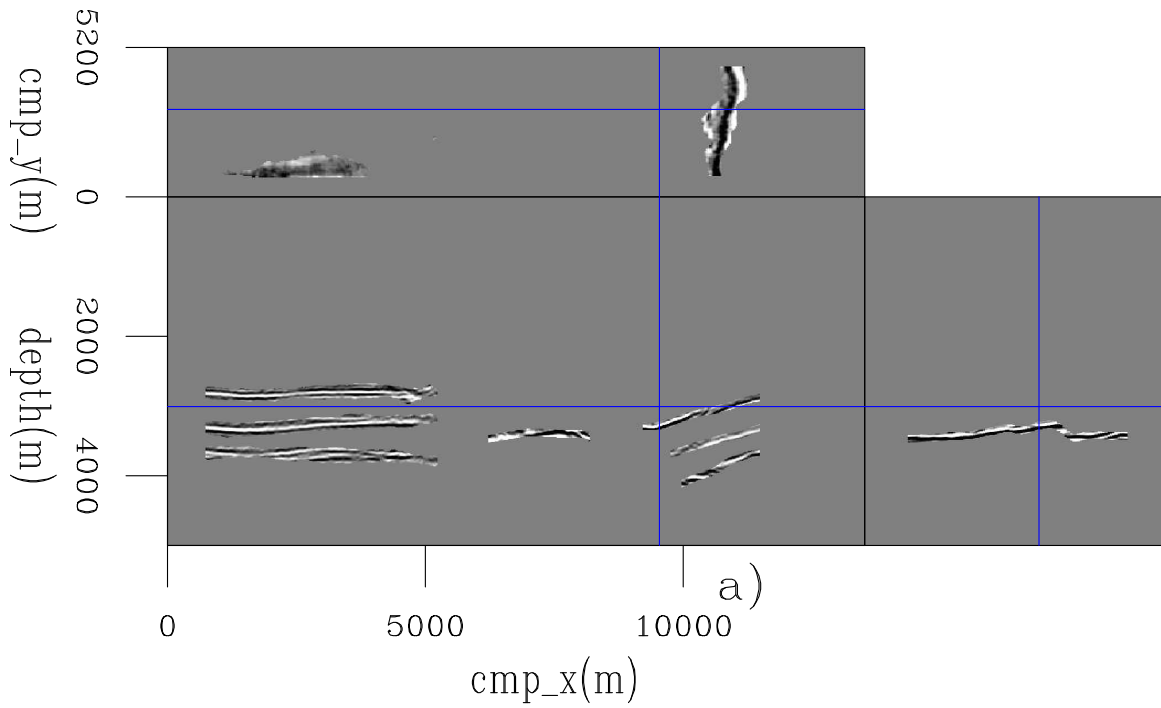


Figure 42: Slices through the windowed prestack image, showing the selected reflectors for the modeling of 30 3D ISPEWs to be used in the sub-salt velocity optimization: a) the zero subsurface offset, and b) the in-line 3520.

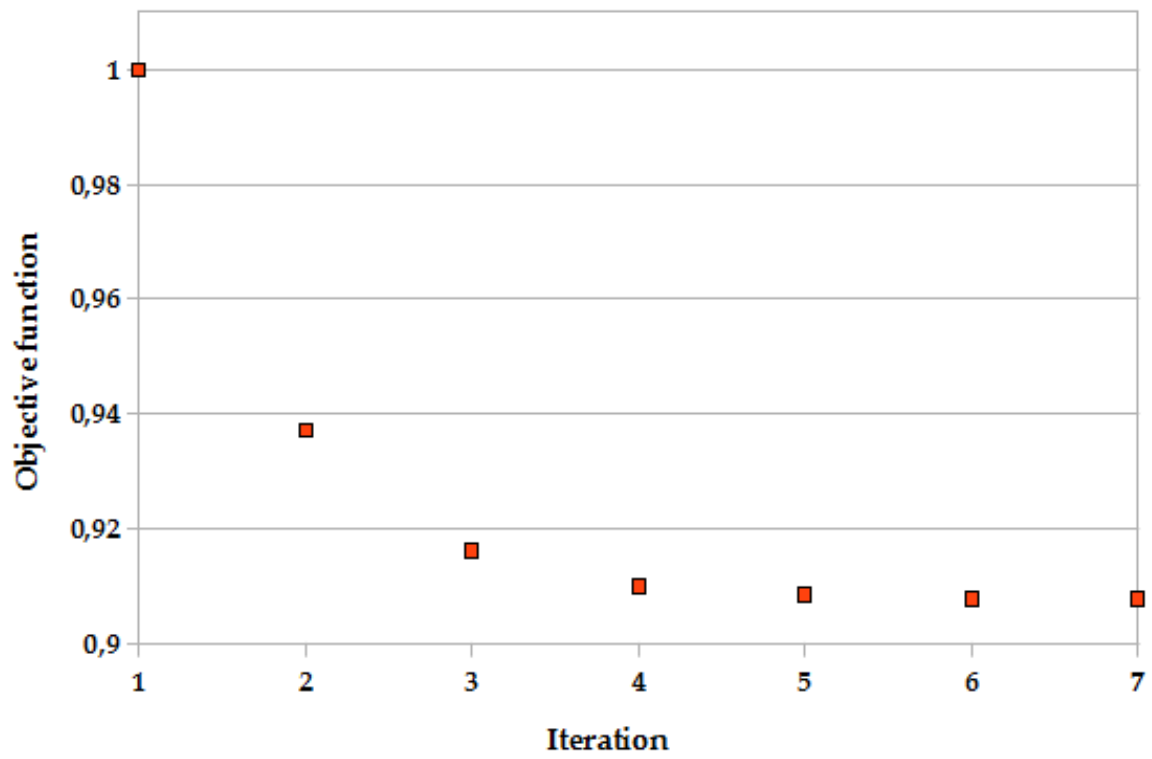


Figure 43: Evolution of the DVSA objective function of the sub-salt velocity optimization.

Guerra and Biondi –

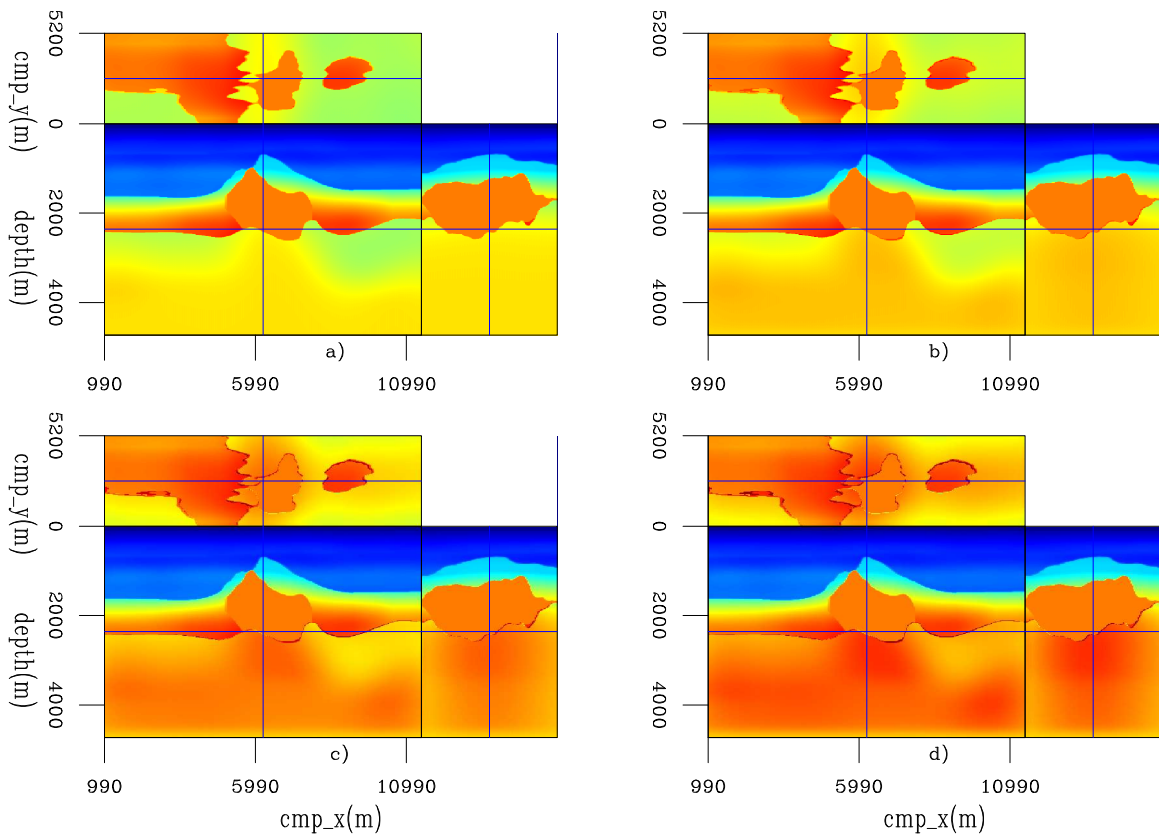


Figure 44: Slices through velocity models for: a) first iteration, b) third iteration, c) fifth iteration, and d) seventh iteration.

Guerra and Biondi –

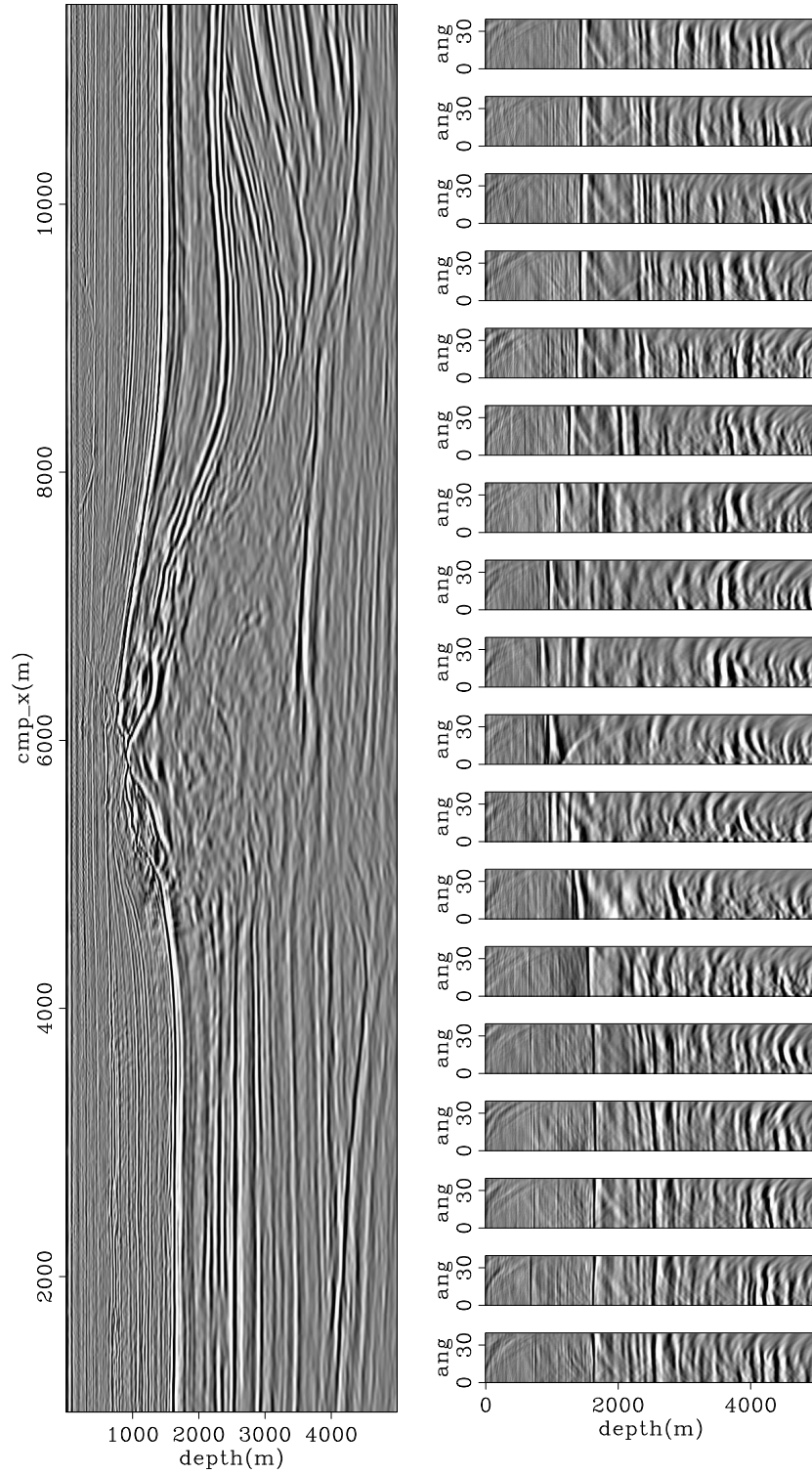


Figure 45: In-line 4060 of the CAM image with the final velocity model after optimization for the chalk layer, salt flooding, and sub-salt velocity optimization. On the top is the zero-subsurface offset section, and at the bottom ADCIGs.

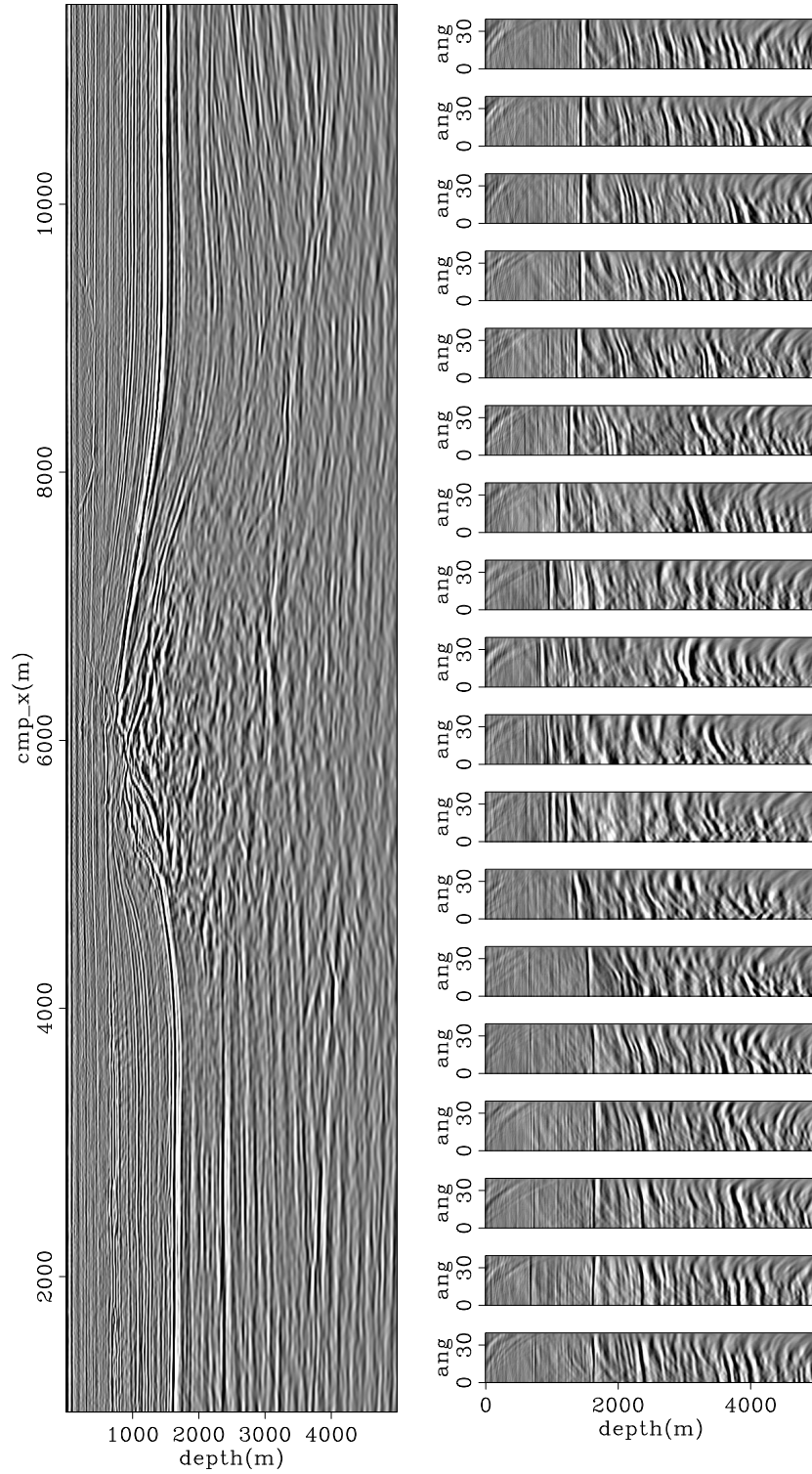


Figure 46: In-line 4060 of the CAM image with the initial velocity model. On the top is the zero-subsurface offset section, and at the bottom ADCIGs.

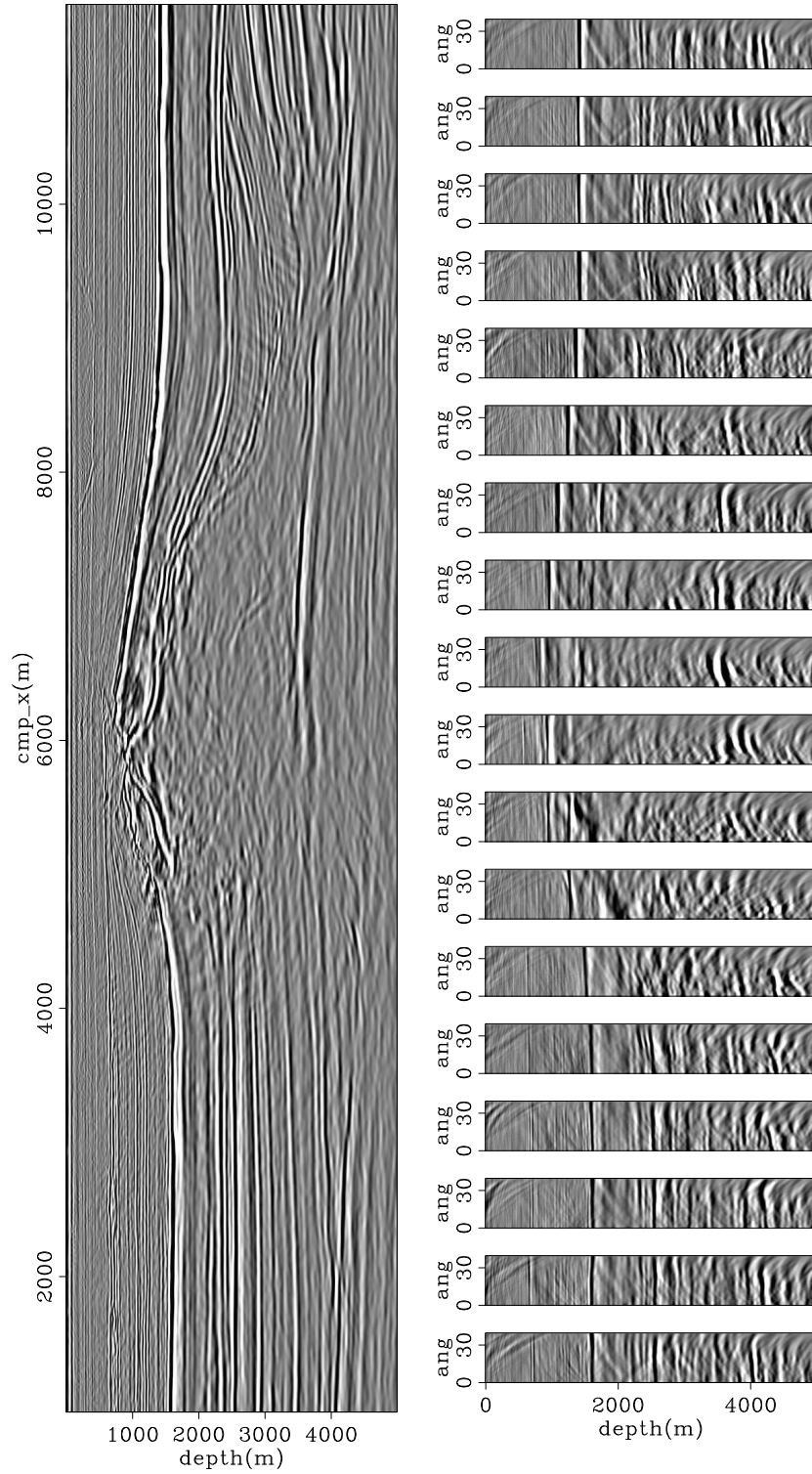


Figure 47: In-line 4060 of the CAM image with the original velocity model. On the top is the zero-subsurface offset section, and at the bottom ADCIGs.

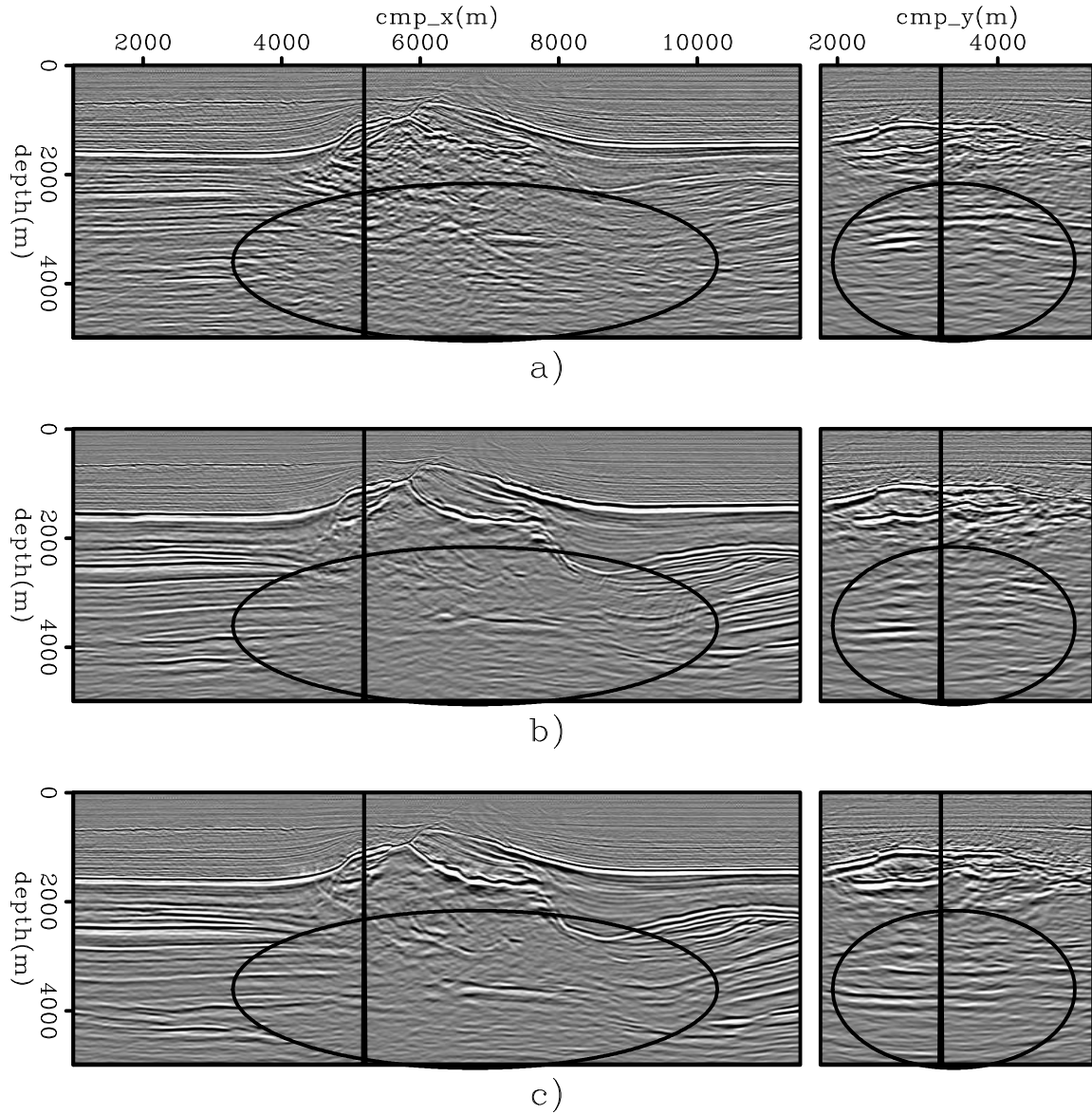


Figure 48: On the left panel is the in-line 3320 and on the right panel is the cross-line 5220 of the CAM images obtained with: a) the initial velocity model, b) the original velocity model, and c) the final velocity model after optimization for the chalk layer, salt flooding, and sub-salt velocity optimization. The oval in the in-line of the final image shows better focusing and continuity for the sub-salt reflectors as well as for the salt flank. Besides focusing and continuity, the oval in the cross-line of the final image shows unstructured sub-salt reflectors not pulled up by velocity errors.

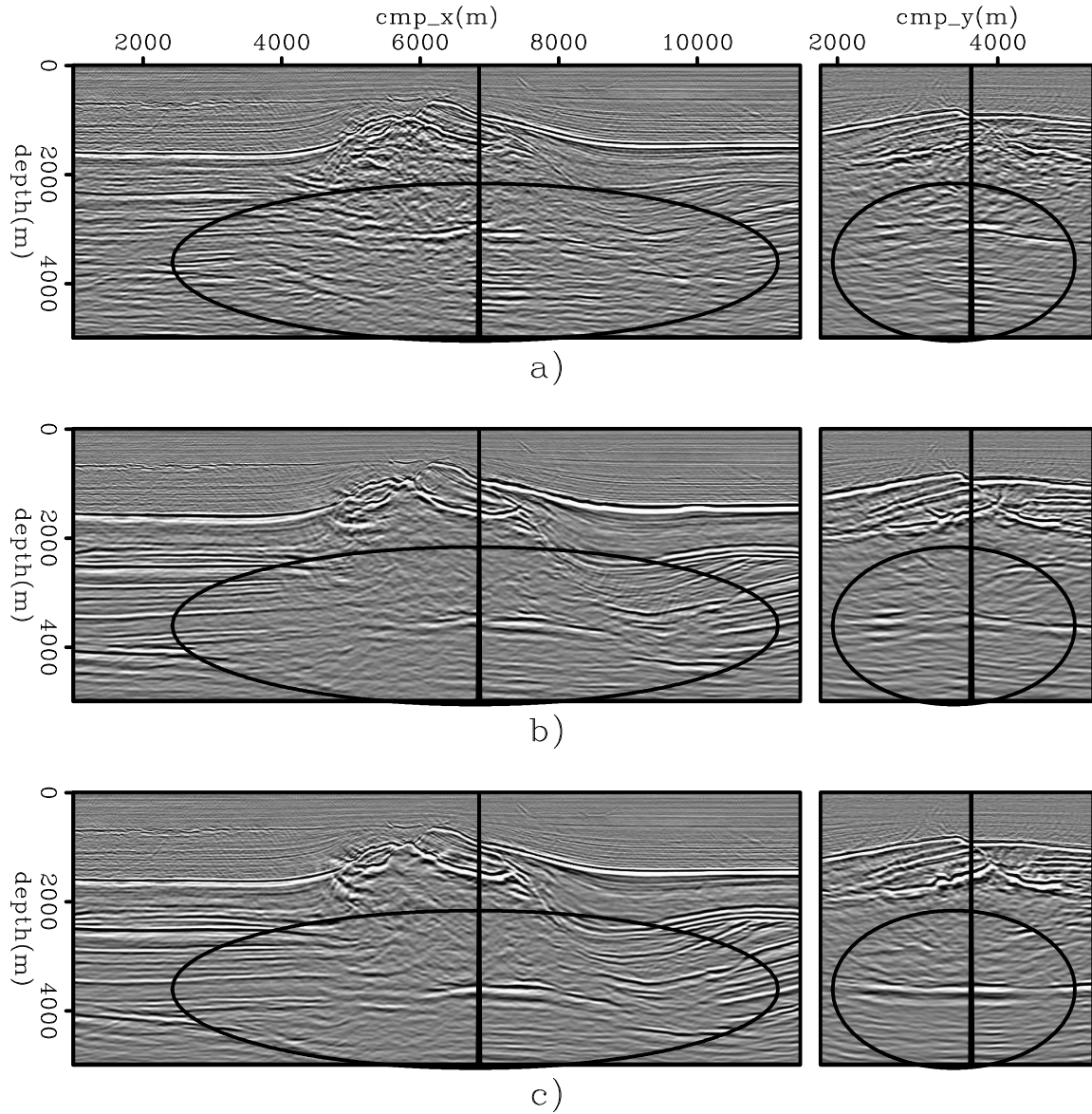


Figure 49: On the left panel is the in-line 3680 and on the right panel is the cross-line 6880 of the CAM images obtained with: a) the initial velocity model, b) the original velocity model, and c) the final velocity model after optimization for the chalk layer, salt flooding, and sub-salt velocity optimization. The oval in the in-line of the final image shows better focusing and continuity for the sub-salt reflectors. Besides focusing and continuity, the oval in the cross-line of the final image shows unstructured sub-salt reflectors not pulled up by velocity errors.

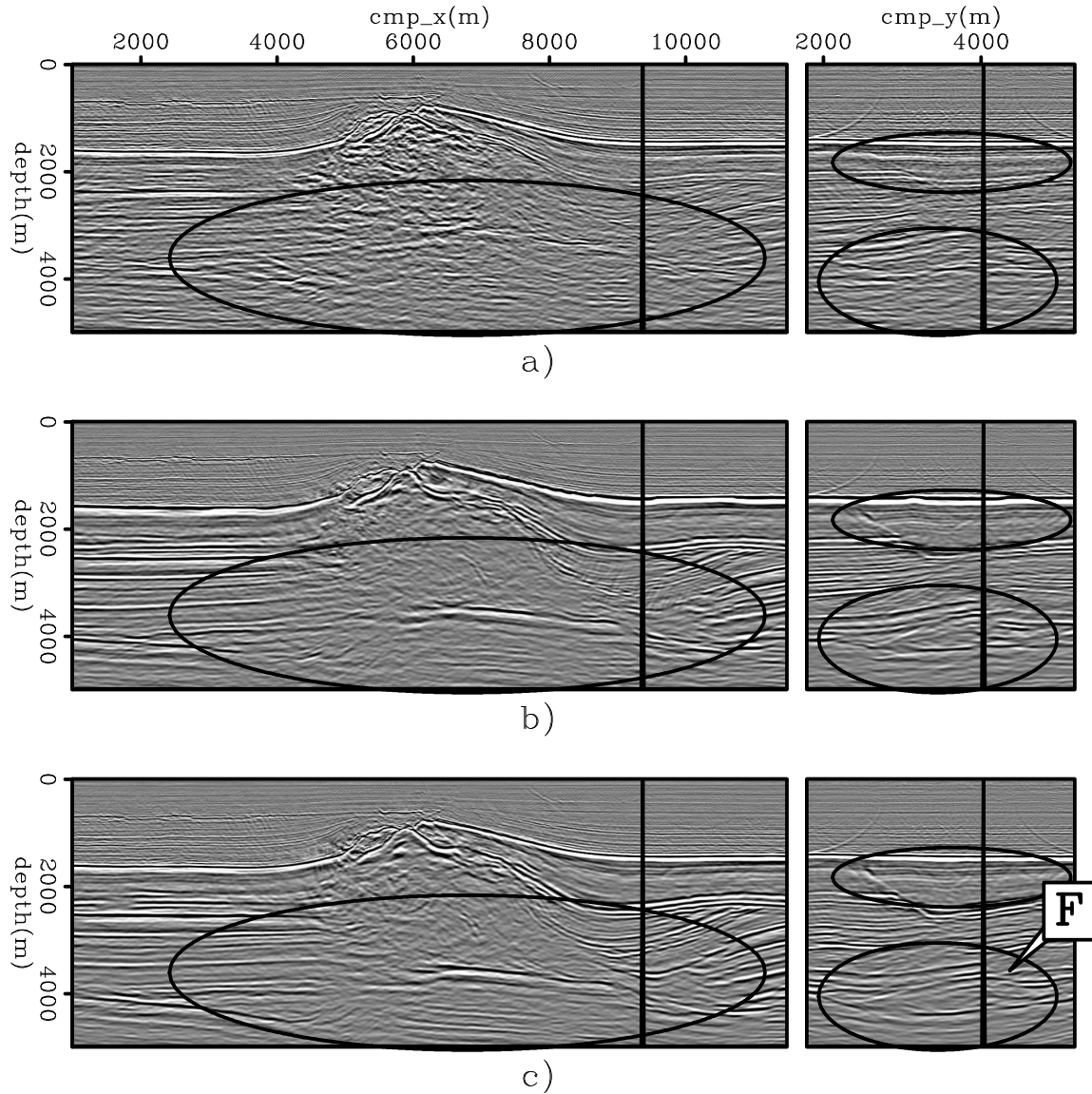


Figure 50: On the left panel is the in-line 4060 and on the right panel is the cross-line 9400 of the CAM images obtained with: a) the initial velocity model, b) the original velocity model, and c) the final velocity model after optimization for the chalk layer, salt flooding, and sub-salt velocity optimization. The oval in the in-line of the final image shows better focusing and continuity for the sub-salt reflectors. In the cross-line, the upper oval of the final image shows better definition of subtle faults in the chalk layer, the lower oval highlights better continuity of the reflectors, and the arrow labeled "F" indicates better fault imaging not clear in the initial and original images.